Ubiquitination of DNA damage-stalled RNAPII promotes transcription-coupled repair

Nakazawa, Y.; Hara, Y.; Oka, Y.; Komine, O.; Heuvel, D. van den; Guo, C.W.; ... ; Ogi, T.

Cell

Article

Ubiquitination of DNA Damage-Stalled RNAPII Promotes Transcription-Coupled Repair

Yuka Nakazawa,[1,2] Yuichiro Hara,[1,2,17] Yasuyoshi Oka,[1,2,17] Okiru Komine,[3,4,17] Diana van den Heuvel,[5,17] Chaowan Guo,[1,2,17] Yasukazu Daigaku,[6,7,17] Mayu Isono,[1,2] Yuxi He,[1,2] Mayuko Shimada,[1,2] Kana Kato,[1,2] Nan Jia,[1,2] Satoru Hashimoto,[1,2] Yuko Kotani,[8,9] Yuka Miyoshi,[3,4] Miyako Tanaka,[10,11] Akira Sobue,[3,4] Norisato Mitsutake,[12] Takayoshi Suganami,[10,11] Akio Masuda,[13] Kinji Ohno,[13] Shinichiro Nakada,[14,15] Tomoji Mashimo,[8,9,16,18] Koji Yamanaka,[3,4,18] Martijn S. Luijsterburg,[5] and Tomoo Ogi[1,2,19,*]

[1]Department of Genetics, Research Institute of Environmental Medicine (RIeM), Nagoya University, Nagoya, Japan
[2]Department of Human Genetics and Molecular Biology, Nagoya University Graduate School of Medicine, Nagoya, Japan
[3]Department of Neuroscience and Pathobiology, Research Institute of Environmental Medicine (RIeM), Nagoya University, Nagoya, Japan
[4]Department of Neuroscience and Pathobiology, Nagoya University Graduate School of Medicine, Nagoya, Japan
[5]Department of Human Genetics, Leiden University Medical Center (LUMC), Leiden, the Netherlands
[6]Frontier Research Institute for Interdisciplinary Sciences, Tohoku University, Sendai, Japan
[7]Graduate School of Life Sciences, Tohoku University, Sendai, Japan
[8]Institute of Experimental Animal Sciences, Graduate School of Medicine, Osaka University, Osaka, Japan
[9]Genome Editing Research and Development (R&D) Center, Graduate School of Medicine, Osaka University, Osaka, Japan
[10]Department of Molecular Medicine and Metabolism, Research Institute of Environmental Medicine (RIeM), Nagoya University, Nagoya, Japan
[11]Department of Immunometabolism, Nagoya University Graduate School of Medicine, Nagoya, Japan
[12]Department of Radiation Medical Sciences, Atomic Bomb Disease Institute, Nagasaki University, Nagasaki, Japan
[13]Division of Neurogenetics, Center for Neurological Diseases and Cancer, Nagoya University Graduate School of Medicine, Nagoya, Japan
[14]Department of Bioregulation and Cellular Response, Graduate School of Medicine, Osaka University, Osaka, Japan
[15]Institute for Advanced Co-Creation Studies, Osaka University, Osaka, Japan
[16]Division of Animal Genetics, Laboratory Animal Research Center, Institute of Medical Science, The University of Tokyo, Tokyo, Japan
[17]These authors contributed equally
[18]These authors contributed equally
[19]Lead Contact
*Correspondence: togi@riem.nagoya-u.ac.jp
https://doi.org/10.1016/j.cell.2020.02.010

SUMMARY

Transcription-coupled nucleotide excision repair (TC-NER) is initiated by the stalling of elongating RNA polymerase II (RNAPIIo) at DNA lesions. The ubiquitination of RNAPIIo in response to DNA damage is an evolutionarily conserved event, but its function in mammals is unknown. Here, we identified a single DNA damage-induced ubiquitination site in RNAPII at RPB1-K1268, which regulates transcription recovery and DNA damage resistance. Mechanistically, RPB1-K1268 ubiquitination stimulates the association of the core-TFIIH complex with stalled RNAPIIo through a transfer mechanism that also involves UVSSA-K414 ubiquitination. We developed a strand-specific ChIP-seq method, which revealed RPB1-K1268 ubiquitination is important for repair and the resolution of transcriptional bottlenecks at DNA lesions. Finally, RPB1-K1268R knockin mice displayed a short life-span, premature aging, and neurodegeneration. Our results reveal RNAPII ubiquitination provides a two-tier protection mechanism by activating TC-NER and, in parallel, the processing of DNA damage-stalled RNAPIIo, which together prevent prolonged transcription arrest and protect against neurodegeneration.

INTRODUCTION

The timely expression of genetic information is crucial for life. However, genomic DNA is continuously damaged, and unrepaired DNA lesions interfere with transcription (Jackson and Bartek, 2009). Eukaryotic cells preferentially remove DNA lesions from the transcribed strand of active genes by transcription-coupled nucleotide excision repair (TC-NER) (Hanawalt and Spivak, 2008). By preventing prolonged stalling of RNA polymerase II (RNAPII) at DNA lesions (Brueckner et al., 2007), TC-NER ensures swift transcription recovery and avoids apoptosis. Individuals suffering from Cockayne syndrome (CS) have defective TC-NER due to mutations in either the *CSA/ERCC8* or the *CSB/ERCC6* gene and display developmental abnormalities, premature aging, and progressive neurodegeneration (Laugel, 2013). These CS clinical features are likely caused by transcriptional misregulation of certain genes (Wang et al., 2014) and cytotoxicity associated with prolonged stalling of RNAPII (Ljungman and Zhang, 1996; Marteijn et al., 2014; Reid-Bayliss et al., 2016; Yamaizumi and Sugano, 1994).

TC-NER is triggered by the stalling of elongating RNAPII molecules (RNAPIIo) at DNA lesions (Xu et al., 2017). The Cockayne syndrome protein complex (CSA/CSB) as well as the UV-sensitive syndrome protein (UVSSA) collaborates in the processing of RNAPIIo and the recruitment of repair factors (Nakazawa et al., 2012; Okuda et al., 2017; van der Weegen et al., 2019). These events trigger the unwinding and excision of the lesion-containing DNA fragment, which is followed by repair synthesis and ligation to complete repair (Aboussekhra et al., 1995). A key event in TC-NER is the recruitment of the TFIIH complex, which is a general transcription factor that also functions in NER. However, it is currently unknown how stalled RNAPIIo molecules transmit a signal to recruit the TFIIH complex to initiate repair and to resume transcription.

One possibility is that the post-translational modification of stalled RNAPIIo is involved in this process. It was indeed described ~20 years ago that the catalytic subunit of RNAPII (RPB1) becomes ubiquitinated in response to DNA damage in both yeast and human cells (Gregersen and Svejstrup, 2018). Extensive studies in yeast *S. cerevisiae* have suggested that the ubiquitination of RPB1 is not required for TC-NER but rather acts in a last-resort pathway that regulates displacement and degradation of DNA damage-stalled RNAPII (Lommel et al., 2000; Nouspikel, 2011; Somesh et al., 2005, 2007; Woudstra et al., 2002). The last-resort pathway acts when TC-NER is not available to allow lesion removal by a slower repair pathway, such as global genome repair (GG-NER) without strand specificity. In humans, the mechanisms involved in the ubiquitination and processing of RNAPII are less well understood. Although several proteins have been linked to RNAPII ubiquitination in human cells (Bregman et al., 1996; Ratner et al., 1998; Nakazawa et al., 2012; Kleiman et al., 2005; Starita et al., 2005; Yasukawa et al., 2008; Anindya et al., 2007), its precise role remains largely unexplored.

In this study, we identify an evolutionarily conserved DNA damage-induced ubiquitination site at K1268 in the RPB1 subunit of human RNAPII; our results reveal that this single RNAPII ubiquitination promotes transcription-coupled repair and protects against neurodegeneration.

RESULTS

RNA Polymerase II Is Predominantly Ubiquitinated at Lysine 1268 of RPB1 after UV

To identify damage-induced ubiquitination sites in human RPB1, the largest subunit of RNA polymerase II (RNAPII), we performed a SILAC-mass spectrometry (MS) in UV-irradiated wild-type (WT) and TC-NER-deficient Δ*UVSSA* HCT116 cells. From the initial MS analysis, we only detected RPB1 ubiquitination at lysine 1268 (K1268) (Table S1). We further performed label-free MS in WT HeLa cells after UV, which revealed additional RPB1 ubiquitination at K1268, K163, K177, K758, K853, and at K1350 (Table S2). All of these RPB1 lysine residues have been reported as putative ubiquitination sites under various conditions (Elia et al., 2015). Importantly, we only robustly detected ubiquitination at K1268 in response to a physiological level of UV-induced DNA damage (Figure 1A).

We generated 15 site-specific knockin mutants in which a single RPB1 ubiquitinated lysine was mutated to arginine (RPB1-KR mutants; Figure 1A) of which 6 sites were identified in our MS, while 9 residues were reported previously (Elia et al., 2015). All KR mutants were successfully generated using CRISPR/Cas9-based gene editing in HeLa cells except for RPB1-K758R (Table S3). We next analyzed the UV-induced ubiquitination of the RPB1-KR mutants (Figure 1B). Importantly, the UV-induced RPB1-IIo top bands (IIo-Ubi) overlapped with immunoblot staining for conjugated ubiquitin (Figure S1A). Moreover, incubation of GFP-tagged RPB1, purified from UV-irradiated HEK293 cells, with the ubiquitin-endoprotease USP2 *in vitro* resulted in loss of the RPB1-IIo top bands and the appearance of cleaved mono-ubiquitin (Figure S1B). These findings demonstrate that these top bands truly represent RPB1-IIo ubiquitination (Bregman et al., 1996; Nakazawa et al., 2012). While most RPB1-KR mutants still showed UV-induced RPB1-IIo ubiquitination, this modification was largely lost in RPB1-K1268R cells (Figure 1B). Notably, RPB1-IIo ubiquitination was also severely diminished in Δ*CSB*, Δ*CSA*, and in Δ*UVSSA* cells (Figures 1B and S3A) (Bregman et al., 1996; Nakazawa et al., 2012; Ratner et al., 1998). Collectively, these data indicate that UV-induced RPB1-IIo ubiquitination occurs predominantly at the K1268 residue. Interestingly, the RPB1-K1268 site is highly conserved (Figure S1C) and is surface-exposed near to where the downstream DNA enters RNAPIIo during transcription (He et al., 2016; Figure S1D).

RPB1-K1268 Ubiquitination Is Essential for Transcription Recovery and UV Resistance

To address the importance of RPB1-IIo ubiquitination, we measured recovery of RNA synthesis (RRS) after UV irradiation, which is a conventional measure of TC-NER activity. While most RPB1-KR mutants exhibited only minor changes, the RPB1-K1268R cells displayed a prominent defect in RRS (Figures 1C and S1E). Importantly, nascent transcript levels (general transcription) were unchanged (Figure S1F) in the RPB1-K1268R cells.

Clonogenic cell survival revealed an increased sensitivity to UV in most of the RPB1-KR mutants, while the RPB1-K1268R cells exhibited the most pronounced UV sensitivity among the mutants (Figure 1D). These results indicate that the ubiquitination of RPB1 at K1268 residue is important for transcription recovery and cell survival after UV-induced DNA damage.

Cullin E3 Ligases Ubiquitinate RPB1 at K1268 and Form K48- and K63-Linked Ubiquitin Chains in Response to UV

To gain insight into the molecular events that mediate RPB1-IIo ubiquitination, we inactivated cullin-ring type E3 ligases (CRLs) with neddylation inhibitor, MLN4924 (Soucy et al., 2009). MLN4924 treatment completely abolished the UV-induced RPB1-IIo ubiquitination, demonstrating that CRLs ubiquitinate the RPB1-K1268 residue (Figure 2A). MLN4924 treatment also diminished RRS in WT cells but not in TC-NER-deficient cells (Figure 2B), implying that CRLs play a predominant role in the RPB1-IIo ubiquitination associated with TC-NER activity.

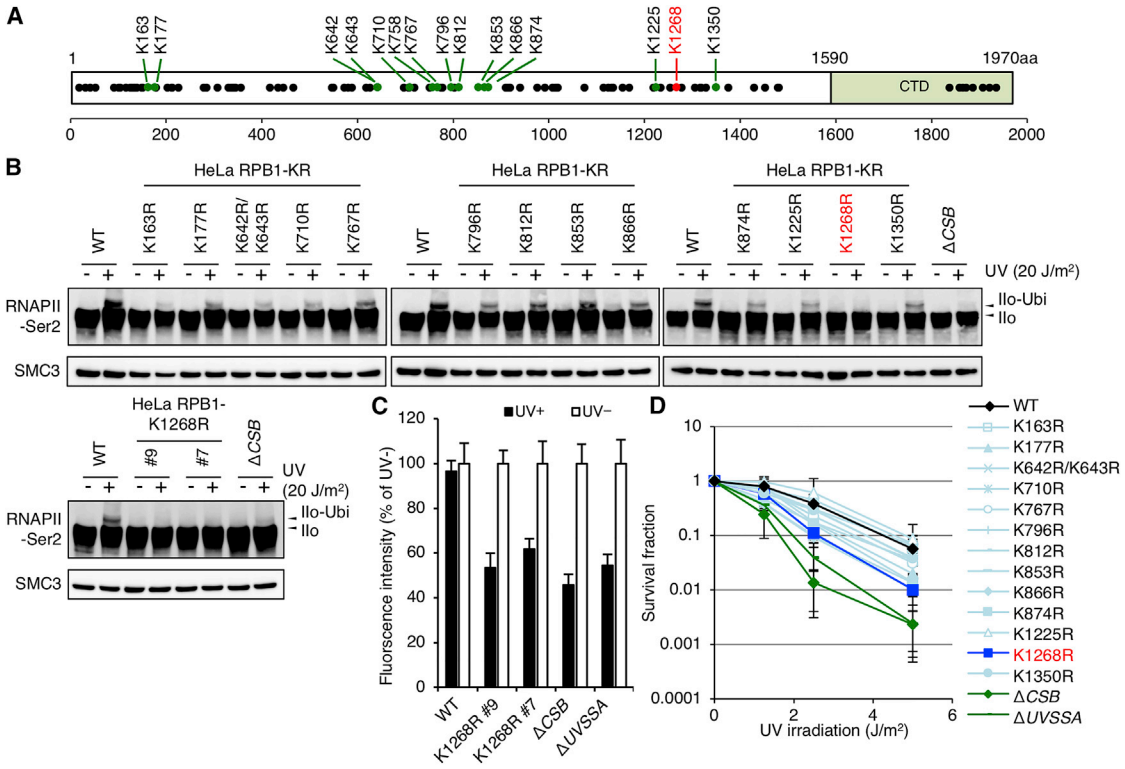

Figure 1. RPB1 Ubiquitination at K1268 Regulates TC-NER and UV Survival

(A) RPB1 ubiquitination sites (black, all lysine residues; green, putative ubiquitination sites; red, K1268).

(B) Detection of the unmodified and ubiquitinated forms (top bands, IIo-ubi) of RNAPIIo in chromatin fraction using the 3E10 antibody in the wild-type (WT), indicated RPB1-KR mutants, and Δ*CSB* HeLa cells at 1 h after UV.

(C) RRS assay in the indicated RPB1-K1268R clones and Δ*CSB* and Δ*UVSSA* HeLa cells. Cells were UV irradiated (closed bars, 5 J/m^2; open bars, without UV), followed by 12 h incubation before 5-ethynyluridine (5-EU) incorporation (Nakazawa et al., 2010). Results for the other RPB1-KR mutants are shown in Figure S1E. Bars represent means and standard deviations (SD) of quintuple wells.

(D) Clonogenic UV survival was measured on the RPB1-KR mutant HeLa cells. black, WT; blue, RPB1-K1268R; green, Δ*CSB* and Δ*UVSSA*; sky blue, KR mutants. Error bars represent SD of triplicate experiments.

See also Figure S1.

We then studied the compositions of ubiquitin chains formed on the RPB1-K1268 residue. Ubiquitin pull-down assays confirmed the UV-induced ubiquitination of RPB1-IIo was severely reduced in Δ*CSA* HeLa cells and abolished in RPB1-K1268R cells (Figure S2). These findings indicate that the ubiquitination of RPB1 primarily occurs on K1268 and is partly dependent on CSA. To investigate which specific ubiquitin chains are formed on RPB1-K1268, Ubiquitin-KR mutants (Ub-K6R, -K11R, -K27R, -K29R, -K33R, -K48R, and -K63R) were expressed in WT HEK293 cells, and ubiquitin pull-down was performed (K27R mutant was not included due to poor expression). Interestingly, we noted substantially reduced total UV-induced RPB1 ubiquitination and increased chain termination products when expressing either Ub-K63R or Ub-K48R (Figure 2C), suggesting that these ubiquitin linkages are primarily formed on RPB1-K1268. The presence of both K48- and K63-linked polyubiquitin chains were confirmed in GFP- RPB1 precipitates from HEK293 cells, and these were fully dependent on K1268 (Figure 2D). Notably, both K48- and K63-linked RPB1 ubiquitin chains were substantially decreased in Δ*CSA* cells (Figure 2D). Taken together, these data indicate that CRLs, including CRL^{CSA}, conjugate K48- and K63-linked ubiquitin chains onto RPB1-IIo at K1268 in response to UV.

Ubiquitination of RPB1-K1268 Is Crucial for the Recruitment of TFIIH after UV

We next set out to define the molecular mechanism through which RPB1-K1268 ubiquitination regulates TC-NER. To this end, we monitored the association of TC-NER factors with ubiquitinated RPB1-IIo by chromatin co-immunoprecipitation (coIP). In WT HeLa cells, RPB1-IIo interacted with CSB and the CRL^{CSA} complex as well as with major subunits of the general transcription factor IIH (TFIIH) core complex and its associated CAK complex in a UV-dependent manner (Figure 3A). Intriguingly, while the RPB1-K1268R interacted normally with CS proteins after UV, its interaction with the core-TFIIH and CAK complexes were severely impaired (Figure 3A). Indeed, the UV-dependent recruitment of TFIIH to RPB1-IIo was completely abolished in Δ*CSA*, Δ*CSB*, or Δ*UVSSA* cells (Figures 3B and S3A), consistent with recent

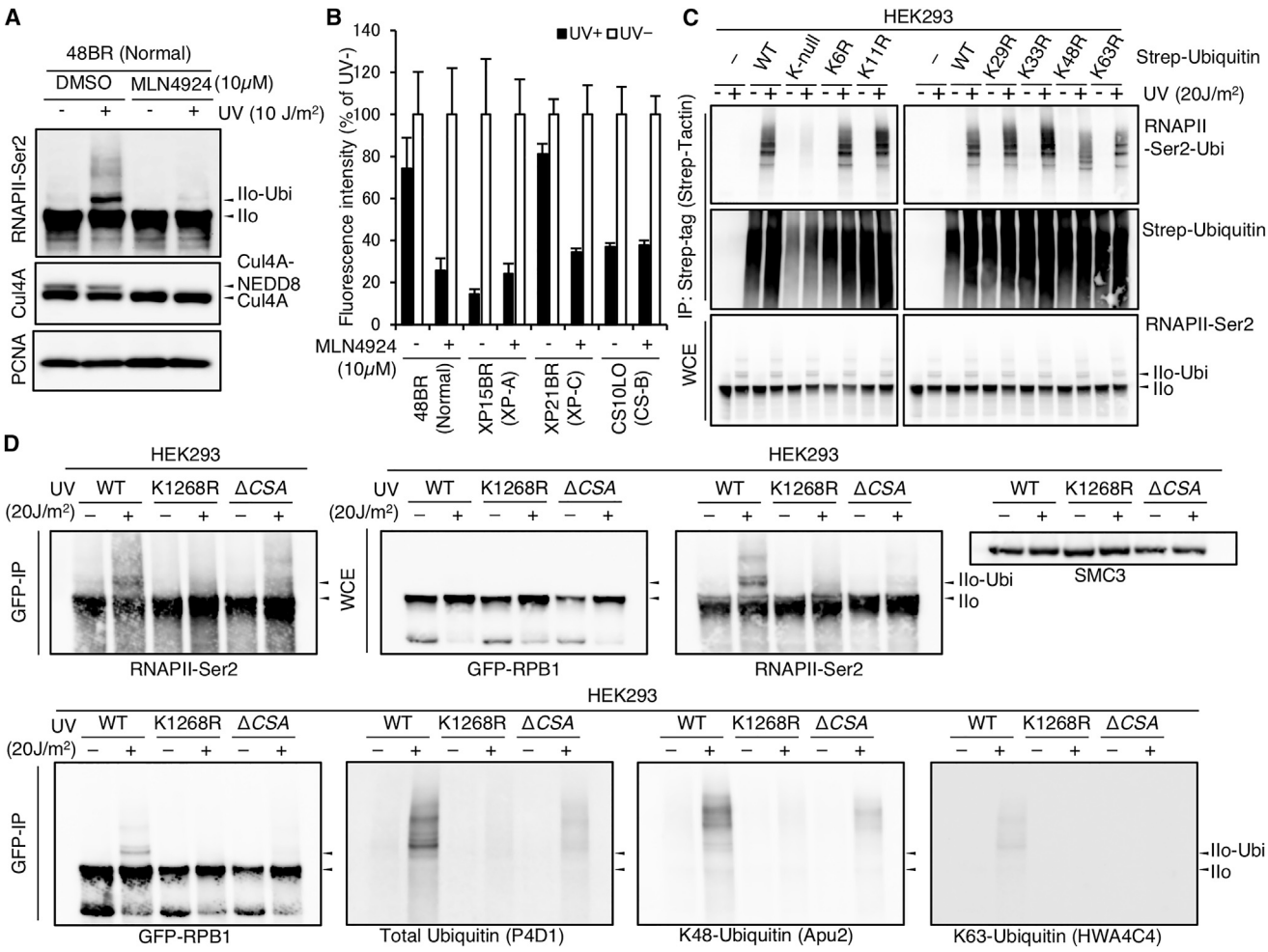

Figure 2. RPB1 Ubiquitination at K1268 Is Dependent on CRL E3 Ligase Activity

(A) RNAPIIo ubiquitination was detected in 48BR fibroblasts treated with or without neddylation inhibitor (MLN4924) for 1 h, followed by UV and further 1 h incubation. Lack of Cullin neddylation was confirmed (Cul4A).

(B) Normal (48BR), GG-NER-deficient (XP-C), TC-NER-deficient (CS-B), and full NER-deficient (XP-A) cells were treated with MLN4924 (+, 10 μM; –, DMSO) for 1 h, followed by RRS measurements after UV (13 J/m^2). Bars represent means (SD) of quintuple wells.

(C) Affinity purification of Strep-Ubiquitin (WT or the indicated KR mutants) from WT HEK293 cells at 1 h after UV. Both ubiquitinated and unmodified RPB1-IIo were detected (RNAPII-Ser2). Ubiquitin chain termination products were detected in cells expressing Ubiquitin-K48R, or -K63R mutants. Total ubiquitinated proteins (Myc-Strep-Ubiquitin) are shown. WCE, whole-cell lysate.

(D) Affinity purification of GFP-RPB1 (WT) from either WT or Δ*CSA* HEK293 cells, or GFP-RPB1 K1268R from WT cells at 1 h after UV.

See also Figure S2.

results (van der Weegen et al., 2019). Importantly, a UV dose-dependent increase in the TFIIH interaction was observed in WT cells but not in RPB1-K1268R cells (Figure 3C). TFIIH also did not associate with RPB1-K1268R at late time points after UV, suggesting an impaired rather than a delayed association (Figure 3D). Moreover, we detected persistent association of CSB/CSA in the RPB1-K1268R mutant at late time points after UV, consistent with defective repair (Figure 3D). We also noticed that the UV-dependent TFIIH interaction was mostly preserved in the other RPB1-KR mutants (Figure S3B). Of note, the TFIIH interaction required for the RPB1 C-terminal domain (CTD)-Ser5 phosphorylation during transcription initiation was normal in the RPB1-K1268R cells (Figure S3C), suggesting that RPB1-K1268 ubiquitination is specifically involved in engaging TFIIH during TC-NER but not during transcription initiation.

Mono-Ubiquitination of UVSSA Transfers TFIIH to RNAPIIo during TC-NER

We next sought to address how RPB1-K1268 ubiquitination is mechanistically linked to the recruitment of TFIIH during TC-NER. We focused on UVSSA because it preferentially binds to ubiquitinated RPB1-IIo after UV irradiation (Nakazawa et al., 2012). In WT cells, we detected the association of endogenous UVSSA with RPB1-IIo after UV, but this was abolished in either Δ*CSA* or Δ*CSB* cells. Conversely, Δ*UVSSA* did not affect the

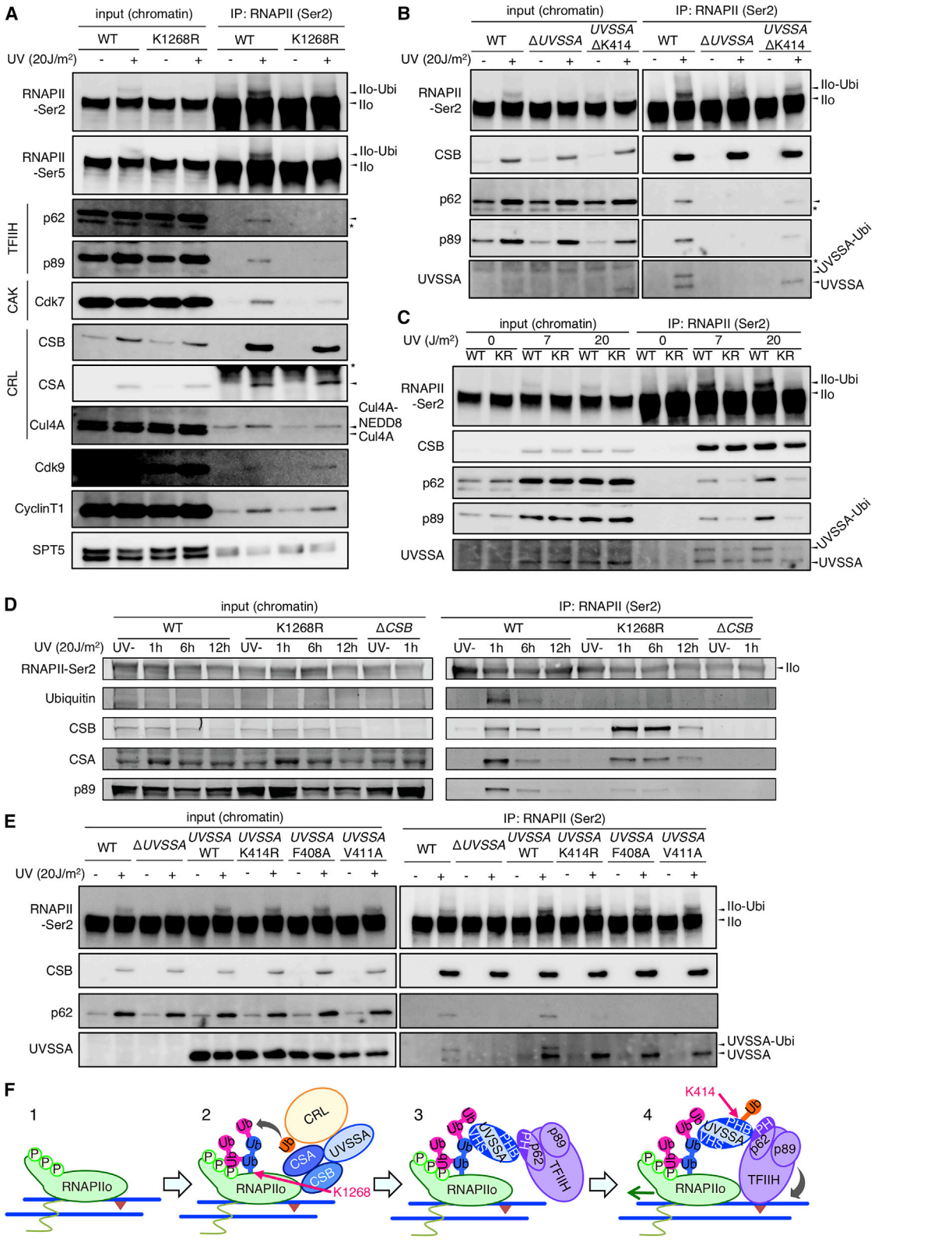

(legend on next page)

association of the CSB/CSA complex with RPB1-IIo (Figures 3B and S3A).

We noticed a distinct UVSSA "mono-ubiquitinated" top band detected in RPB1-IIo immunoprecipitates after UV (Figure 3B). MS analyses revealed that UVSSA mono-ubiquitination occurs mainly at K414 (our unpublished data; Higa et al., 2018). The mono-ubiquitinated UVSSA disappeared in RPB1-IIo immunoprecipitates in HeLa cells lacking the UVSSA-K414 residue (ΔK414; Figure 3B). These findings identify K414 as the key mono-ubiquitination site in UVSSA in response to UV. Strikingly, the interaction between UVSSA and RPB1-IIo was significantly reduced in the RPB1-K1268R cells, and this particularly affected the mono-ubiquitinated form of UVSSA (Figures 3C and S3C). Although difficult to detect, it appeared that general levels of UVSSA-K414 ubiquitination were mostly unaffected in RPB1-K1268R cells. Interestingly, this K414 residue is located within a stretch of acidic residues in the central region of UVSSA (390–430 aa), which directly interacts with the core-TFIIH-p62 pleckstrin homology (PH) domain (Okuda et al., 2017). To specify critical residues in UVSSA that mediate the TFIIH-p62 recruitment to ubiquitinated RPB1-IIo, we generated Δ*UVSSA* HeLa cells stably expressing the UVSSA-K414R, as well as the PH domain-binding site (PHB) mutants (Okuda et al., 2017). The UV-dependent TFIIH-p62 recruitment to RPB1-IIo was severely compromised in *UVSSA*-ΔK414 cells (Figure 3B), as well as in UVSSA-K414R cells (Figure 3E), indicating that the UVSSA-K414 ubiquitination is important for the TFIIH recruitment. As expected, the UVSSA-PHB mutants also displayed defects in the TFIIH recruitment (Figure 3E). Strikingly, while the PH domain-mediated UVSSA-TFIIH interaction was indeed impaired in the UVSSA-PHB mutants, we detected a normal interaction between the UVSSA-K414R mutant and TFIIH-p62 (Figure S3D). Importantly, RRS was impaired in all of the UVSSA mutants (Figure S3E), showing that the UVSSA-K414 ubiquitination and the TFIIH-p62 interaction are both critical for TC-NER. Notably, RPB1-IIo ubiquitination was restored to the WT level in all these UVSSA mutant cells (Figure 3E) despite their TC-NER defect.

These findings indicate that the damage-induced RNAPIIo ubiquitination mainly occurs prior to the recruitment of UVSSA and TFIIH, and that the ubiquitination of UVSSA-K414 is exclusively needed for the efficient transfer of TFIIH from UVSSA to stalled RNAPIIo (Figure 3F), which may involve later displacement of p62 by other NER proteins, such as XPG (xeroderma pigmentosum, complementation group G protein).

Genome-wide ChIP-Seq Reveals a Strong Transcription Recovery Delay in the RPB1-K1268R Mutant

To study the consequence of impaired RPB1-K1268 ubiquitination on a genome-wide scale, we employed chromatin immunoprecipitation of RPB1 to capture DNA fragments, which were analyzed by next-generation sequencing (NGS) (chromatin immunoprecipitation sequencing [ChIP-seq]: Figure 4A). This enables the quantitative and spatiotemporal mapping of RNAPII in the genome. We performed ChIP-seq in WT and RPB1-K1268R mutant HeLa cells using antibodies against total RPB1, or CTD phosphorylation-specific RPB1 (Figure 4A). Without UV irradiation, in agreement with previous reports (Brookes et al., 2012; Odawara et al., 2011; Rahl et al., 2010), CTD-Ser5-phosphorylated RPB1 (RPB1-Ser5) formed two distinct peaks near transcription start sites (TSSs), which reflect RNAPII molecules during transcription initiation and promoter-proximal pausing (Figure 4B, right panel gray lines). CTD-Ser2-phosphorylated RPB1 (RPB1-Ser2), which represents the elongating form of RNAPII, was distributed throughout gene-bodies and was significantly enriched after transcription end sites (TESs) due to post-transcriptional pausing prior to dissociation (Figure 4B, left panel gray lines). Total RPB1 ChIP profiles (pan-RPB1) were a composite of RPB1-Ser2 and RPB1-Ser5 features (Figure S4A, right panels gray lines). Importantly, all these RNAPII distribution profiles were identical between RPB1-WT and RPB1-K1268R mutant in undamaged cells (Figures 4B and S4A), demonstrating that RPB1-K1268 ubiquitination does not affect general transcription.

At 3 h after UV, the distribution of RNAPII was comparable between RPB1-WT and RPB1-K1268R and significantly shifted with increased enrichment near the 3′ of TSS concomitant with a reduction at post-transcriptional pausing sites (PTPSs) after the TES (Figure 4B, green lines). This suggests that fewer RNAPII molecules reach the end of genes due to DNA damage-induced transcription arrest, stalling or pausing, in agreement with previous analyses (Paulsen et al., 2014). Strikingly, while the RNAPII distribution started to shift back at 12 h after UV in WT cells, the RPB1-K1268R mutant showed impaired transcription recovery (Figure 4C). These profile differences were

Figure 3. TFIIH Recruitment Is Dependent on the Ubiquitination of RPB1-K1268 and UVSSA-K414

(A) CoIP with RNAPII-Ser2 antibody (Ab5095) at 1 h after with or without UV from the chromatin fraction of WT or RPB1-K1268R (K1268R) HeLa cells. The input is 1.5% of the chromatin fraction. RNAPII was detected with 3E10 (Ser2) and 3E8 (Ser5) antibodies. Asterisks represent non-specific products. Results for the other RPB1-KR mutants are shown in Figure S3B.

(B) CoIP as in (A) from WT, Δ*UVSSA*, or *UVSSA* knockin with a K414 deletion (ΔK414) HeLa cells at 1 h after UV irradiation. No UVSSA ubiquitination was detected in the ΔK414 cells.

(C) CoIP as in (A) from WT or RPB1-K1268R HeLa cells at 1 h after UV irradiation. Note that the amount of ubiquitinated UVSSA interacting with RPB1-IIo was reduced in RPB1-K1268R mutant.

(D) CoIP as in (A) from the indicated HeLa cells (WT, RPB1-K1268R, Δ*CSB*) after UV, followed by incubation for the indicated time periods. FK2 antibody detects ubiquitinated RPB1-IIo in WT cells.

(E) CoIP as in (A) from the indicated HeLa cells (WT, Δ*UVSSA*, and Δ*UVSSA* with ectopic expression of the indicated V5-tagged *UVSSA* variants) at 1 h after UV irradiation. UVSSA K414 ubiquitination is critical for the TFIIH recruitment.

(F) Working model for the recruitment of TFIIH. 1: RNAPIIo stalls at DNA damage. 2: The CRL^{CSA} complex, possibly in concert with another E3 ligases ubiquitinates RPB1-K1268; UVSSA is also recruited by CSB/CSA. 3: VHS domain supports the UVSSA interaction with ubiquitinated RPB1-IIo; UVSSA recruits TFIIH-p62 via PH-domain binding sequence (PHB). 4: Mono-ubiquitination of UVSSA-K414 facilitates transfer of TFIIH to RPB1-IIo.

See also Figure S3.

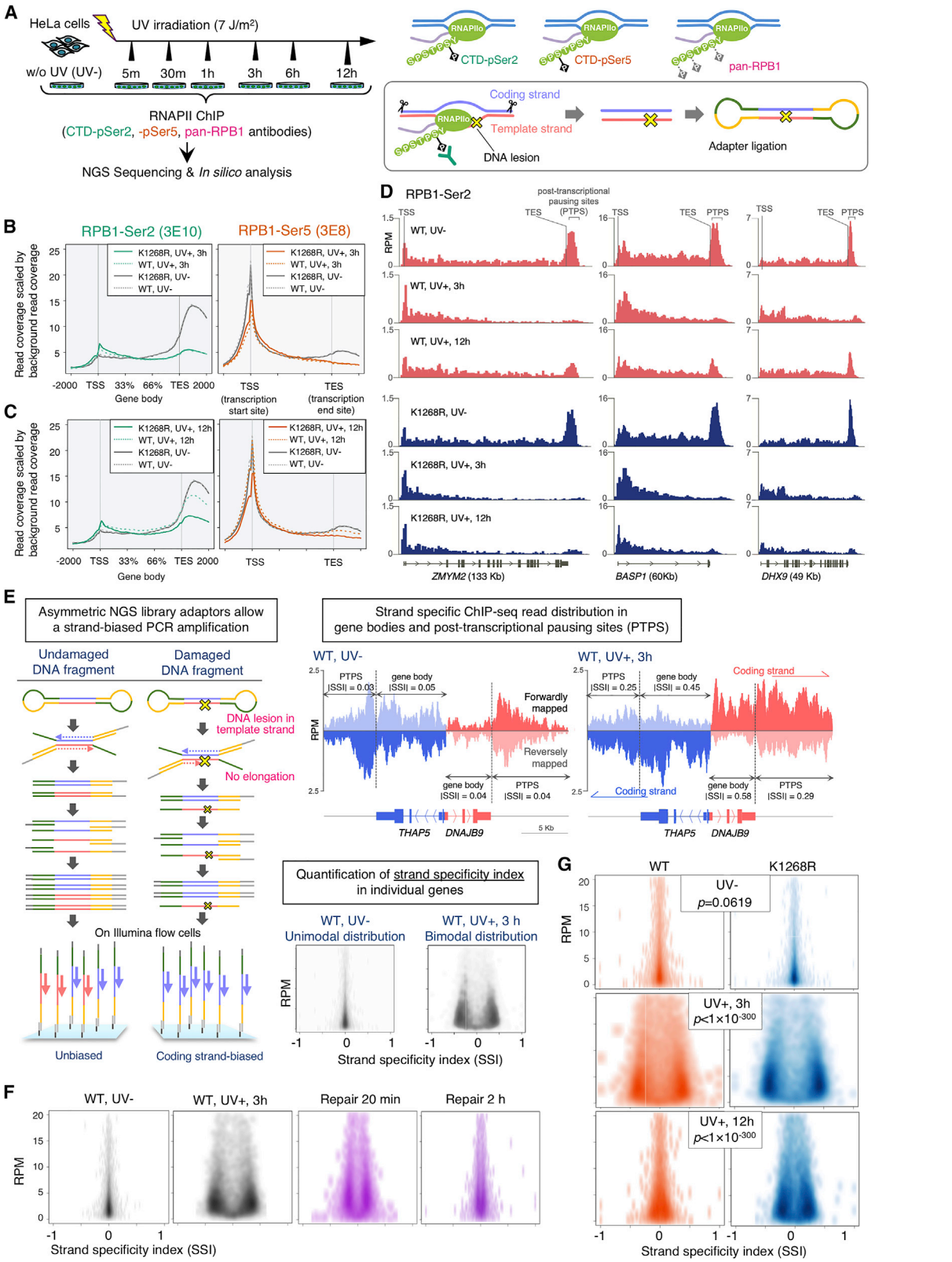

(legend on next page)

also prominent in individual genes (Figure 4D). Importantly, TC-NER-deficient cells showed a similar RNAPII distribution to the K1268R mutant at all time points analyzed except 3 h (Figures S4A and S4B; see arrows in RPB1-Ser2 3 h panels), suggesting this reflects the degree of impaired TC-NER.

Strand-Specific ChIP-Seq Identifies RPB1-IIo Stalled at DNA Damage and Demonstrates Slow Repair Kinetics in RPB1-K1268R Mutant in Most Genes

We next sought to establish a new ChIP-seq method measuring genome-wide TC-NER kinetics. This method relies on the principle that a fraction of the DNA fragments prepared after RPB1-Ser2 ChIP contain DNA lesions in the transcribed strand, which caused RNAPIIo to stall in the first place. These DNA lesions will prevent PCR amplification during the generation of NGS libraries. However, the asymmetric structure of the Illumina library adapters (Figure 4E, left panel) allows the strand-specific PCR amplification of fragments without DNA damage resulting in the enrichment of reads in the coding (non-transcribed) strands. Indeed, a shift in strand-biased ChIP-seq reads was clearly detected in UV irradiated samples, and this strongly correlated with gene orientation (Figure 4E, top-right panel).

To estimate gene-by-gene repair kinetics from the strand-biased ChIP-seq data, we calculated the strand-specificity index (SSI), which reflects the degree of remaining DNA damage in transcribed strands in individual genes (see STAR Methods). Transcription arrests at DNA lesions in gene bodies contribute to an increase in the absolute values of SSI (|SSI|), whereas RNAPIIo molecules pause after transcription at the PTPSs do not (Figure 4E, top-right panel). Plotting the SSI against the read coverage within "gene bodies" in individual "active genes" (9,836 genes, Figure S4C) revealed a unimodal distribution in undamaged HeLa cells (no strand-bias) (Figure 4E, bottom-right panel). Conversely, UV irradiation triggers a bimodal SSI distribution due to bidirectional transcription and the stalling of RNAPIIo. Importantly, treating ChIPed DNA fragments from UV-irradiated cells with a DNA repair enzyme mix (preCR, NEB) prior to library preparation fully reverted the bimodal SSI pattern to a unimodal distribution (Figure 4F). Thus, the strand specificity is a true consequence of the presence of UV-induced DNA lesions.

We calculated the SSI to evaluate the impact of RPB1-K1268 ubiquitination on DNA repair kinetics in individual genes. In WT cells, SSI plots shifted to a bimodal distribution at 3 h post-UV irradiation, which returned to a unimodal distribution within 12 h, indicating completion of DNA repair within this time frame in "most genes" (Figure 4G, WT, red). In contrast, the bimodal distribution remained in the RPB1-K1268R mutant up to 12 h after UV, reflecting a significant delay in the genome-wide removal of DNA lesions by TC-NER (Figure 4G, K1268R, blue). To further support this conclusion, we calculated the SSI in TC-NER-deficient cells. Importantly, we first confirmed that the RPB1-Ser2 ChIP-seq read depths of individual genes showed a good correlation between biological replicates in all tested cells (Figure S4D). Indeed, all of these TC-NER-deficient cells displayed a bimodal distribution of SSI at 12 h after UV, indicating impaired removal of DNA lesions in most genes in these cells (Figure S4E). In conclusion, our genome-wide analysis supports an important role for RPB1-K1268 ubiquitination in TC-NER-mediated clearing of DNA lesions from transcribed-strands of active genes. In principle, this method can also be applied for the detection of genome-wide RNAPII molecules stalled at various types of other transcription-blocking DNA lesions, such as cisplatin and Illudin S.

A Detailed TC-NER Repair Kinetic in the RPB1-K1268R Mutant

Our strand-specific ChIP-seq method overcomes known limitations in conventional methods (Mayer et al., 2017) and enable the evaluation of gene-by-gene repair kinetics. Indeed, analysis of individual genes (see *MCM3* in Figure 5A) revealed slower repair kinetics in RPB1-K1268R cells compared to WT.

To extend our gene-by-gene analysis further, we calculated the recovery index (RI), which represents the progression of DNA lesion removal from transcribed-strands in the entire genome

Figure 4. Strand-Specific ChIP-Seq Enables Precise Spatiotemporal Mapping of RPB1-IIo Molecules Stalled at DNA Damage Sites

(A) Schematic representation of RNAPII ChIP-seq, which was performed with anti-RPB1 phospho-CTD-specific antibodies. After decrosslinking, DNA lesions remain in the template strand. Strand-specific NGS libraries were prepared for the Illumina platform (see also E).

(B and C) Distributions of chromatin-bound RNAPII (RPB1-Ser2, 3E10; -Ser5, 3E8) within gene bodies and flanking regions (B) 3 or (C) 12 h after 7J/m^2 UV irradiation in either WT or RPB1-K1268R HeLa cells. Note that no obvious difference in RNAPII distribution was observed between WT and RPB1-K1268R mutant without UV (gray lines). Without UV, data are identical in (B) and (C). Additional plots for other time points, for pan-RPB1, and for TC-NER-deficient cells are shown in Figures S4A and S4B.

(D) RNAPIIo distribution changes in individual genes after UV irradiation. RPB1-Ser2 ChIP-seq read coverages (RPM, reads per million mapped reads) in representative genes in (B) and (C) are shown.

(E) Schematic representation of the strand-specific ChIP approach (RPB1-Ser2, 3E10). Calculation of the strand-specificity index (SSI) is detailed in STAR Methods. Left panel: the asymmetric adapters for Illumina libraries allow preferential amplification of DNA strands without damage, resulting in a retention of directional information (see also A). Top-right panel: strand-biased ChIP-seq reads associated with the gene orientation are shown for representative genes. Without UV, RPM of forwardly mapped reads and reversely mapped reads are similar and no strand specificity is detected (absolute SSI value, |SSI| = 0). At 3 h after UV, |SSI| increases due to the presence of DNA lesions in the transcribed strand. Bottom-right panel: scatterplots of SSI against RPM within gene bodies in individual "active genes" (9,836 genes, see definition in Figure S4C). Unimodal SSI distribution is observed in a representative sample without DNA damage, while bimodal distribution appears 3 h after UV irradiation. Plots reused in (G). Number of mapped reads within +301 bp to +2 kb was counted for RPM in the plots.

(F) ChIPed DNA (RPB1-Ser2, Ab5095) from UV-irradiated (3 h after 7 J/m^2) WT HeLa cells was treated with DNA damage repair enzyme mix for 20 min, or 2 h prior to library preparation. Note that the bimodal distribution disappeared (purple).

(G) SSI scatterplots of active genes in WT (red) or RPB1-K1268R (blue) HeLa cells after UV irradiation (7 J/m^2) based on strand-specific ChIP-seq (RPB1-Ser2, 3E10). All the plots employed active genes. Plots reused in Figure S4E. p values were calculated with the Wilcoxon signed-rank test (n = 9,836) and were corrected by the Benjamini-Hochberg method. Scatterplots of the samples from other time points, as well as TC-NER-deficient cells are shown in Figure S4E.

See also Figure S4.

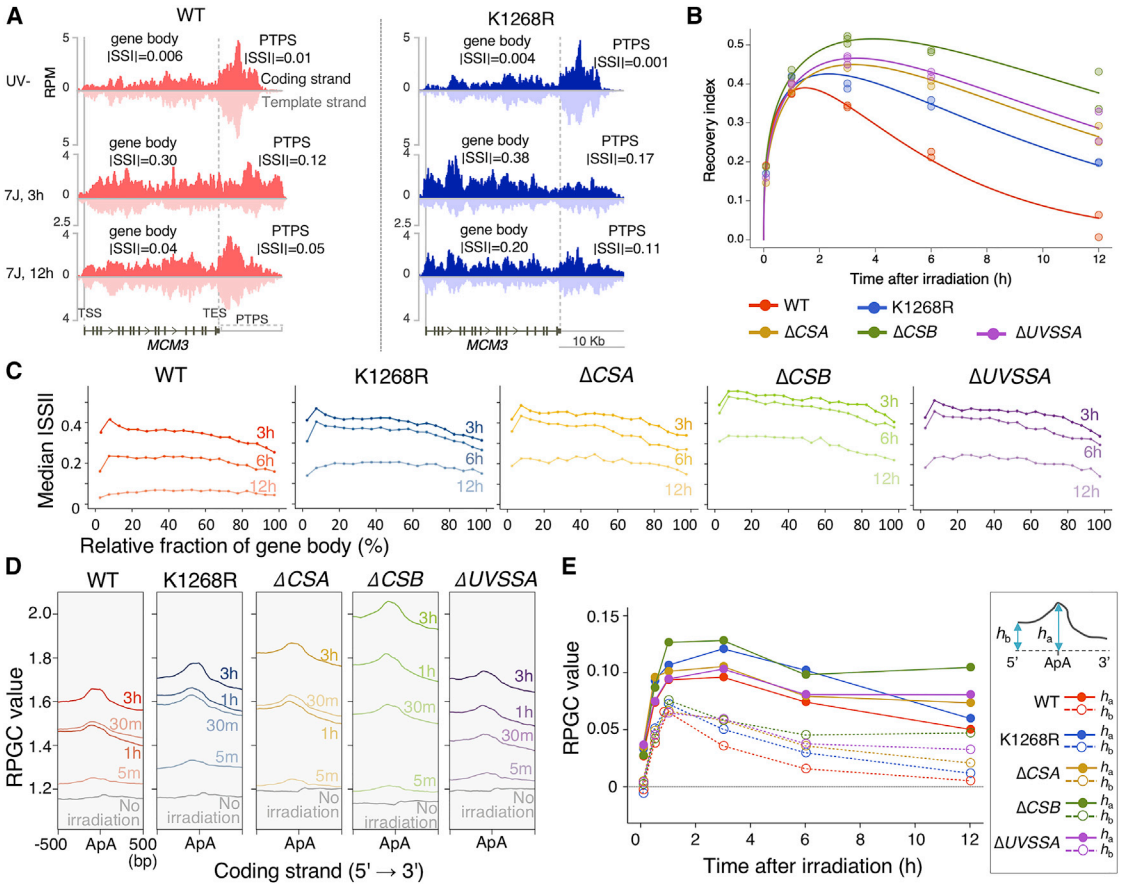

Figure 5. Slow DNA Repair Kinetics of Transcribed Strands in RPB1-K1268R Mutant

(A) Strand-specific ChIP-seq (RPB1-Ser2, 3E10) read distribution in a representative gene (*MCM3*) showing slow repair kinetics in RPB1-K1268R (blue) compared to WT (red) cells after UV (7 J/m^2). |SSI| calculated for *MCM3* gene body and PTPS regions are indicated.

(B) Time course in the indicated HeLa cells of the recovery index (RI), representing the progression of DNA lesion removal from transcribed strands in the entire active genes. The RI is derived from a mixture of Gaussians that correspond to the unrepaired gene fractions (i.e., |SSI| < > 0) in the gene-by-gene SSI distribution of RPB1-Ser2 ChIP-seq (3E10) (see also Figure S5A). The RI was calculated from duplicate time-course experiments shown in Figures 4G and S4E, and the curves were fitted to gamma functions.

(C) Time course of median |SSI| across relative position in gene bodies in whole active genes. In this analysis, central genic region (>20 kb active genes) were used in order to exclude the effects of mapped reads nearby TSS and TES. This selection did not affect the RI kinetics (See Figure S5B). No positional preference of damage removal from gene bodies was detected. SSI data are same as in (B). Results of early time points after UV irradiation are shown in Figure S5D (3 h data replotted).

(D) Time course of RNAPIIo accumulation at T-T dimer sites. Mapped reads enrichments in the coding strand (ApA, A < > A) are shown (central genic region of >20 kb active genes). Colored humps represent delayed T-T dimer removal in RPB1-K1268R mutant and TC-NER-deficient cells. ChIP-seq data are same as in (B). Results of late time points after UV irradiation are shown in Figure S5F (3 h data replotted). RPGC (reads per genome coverage) represents 1× depth of coverage.

(E) Asymmetric distribution of the mapped reads in the coding strand immediately adjacent to A < > A dimer sites (h_a) and in the 5′ lesion-proximal region (h_b) shown for the central genic region of >20 kb active genes in chr 1 (left panel). Note that the base line at the 5′ lesion-proximal region (h_b) is higher than that at the 3′ side, indicating stalling of RPB1-IIo at the DNA lesion causing queueing of multiple RNAPIIo. The queue formation kinetics is identical in all cell types, while the resolution is fastest in WT (dashed lines). Data in (D) (Figure S5F) are analyzed.

See also Figure S5.

(see STAR Methods and Figure S5A). To exclude the effects of RNAPII pausing near TSSs, TESs, and PTPSs, from now on we focused on the "central genic region" in 5,704 active genes. This selection from 5 kb downstream of the TSS to 5 kb upstream of the TES of >20 kb active genes did not affect the RI kinetics (Figures 5B and S5B). After reaching a maximum at 1 h post-UV irradiation, WT HeLa cells showed a gradual decrease in RI within 12 h indicative of near-complete repair within this time frame. However, the RI remained high in RPB1-K1268R and TC-NER-deficient cells indicative of incomplete repair (Figure 5B). Surprisingly, Δ*CSB* cells displayed slower repair kinetics compared to the other cells, which possibly reflects slow repair of UV-induced oxidative DNA damage (Menoni et al., 2018). The RPB1-K1268R cells showed significantly impaired TC-NER activity throughout the genome albeit not as strong as complete loss of TC-NER.

As the average transcription speed is estimated to be ~2.5 kb per min and 7 J/m^2 UV irradiation triggers ~1 lesion per 10 kb, it would be expected that all sparsely running RNAPIIo reach DNA

lesions within the first ~10 min post-UV irradiation. However, the RI increases in the first 1–3 h, suggesting a slowdown of the transcription elongation rate after UV. The total number of reads did not decline after UV, while the strand bias increased in the first 3 h (Figure S5C), indicating that the RI kinetics truly represent progression of DNA lesion removal from transcribed strands.

Spatial Distribution of Stalled RNAPIIo Molecules Associated with TC-NER

We next examined the SSI across relative positions in genes. This analysis revealed that DNA lesions were uniformly removed from entire gene bodies in WT cells (Figures 5C and S5D), suggesting that TC-NER is initiated simultaneously by sparsely running RNAPIIo molecules that stall at DNA lesions. Interestingly, the concordant increase of SSI was observed in all cell types at early time points post-UV irradiation (Figure S5D), suggesting that *de novo* collisions of sparsely running RNAPIIo with DNA damage continuously occurred within 1 h after UV in all cell types, while further stalling continues afterward in repair-deficient cells.

We next attempted a base-resolution mapping of DNA damage-stalled RNAPIIo. UV irradiation predominantly generates transcription-blocking cyclobutane pyrimidine dimers (CPDs) in DNA (Friedberg et al., 2005). An abundance of mapped reads in the coding strands near A < > A dimers could indeed be successfully detected in WT HeLa cells after UV (Figure S5E), due to the stalled RNAPIIo at UV-induced T-T CPDs in transcribed strands. We further analyzed the RNAPIIo stalling at base resolution in TC-NER-deficient as well as RPB1-K1268R cells (Figures 5D and S5F). Interestingly, we noted an asymmetry in the mapped reads near A < > A dimer sites in the coding strand (T < > T DNA damage in the opposite transcribed strands), suggesting increased accumulation of RNAPIIo at the 5′ compared to the 3′ lesion-proximal region in RPB1-K1268R cells as well as in TC-NER-deficient cells (Figure 5D). The increase of reads immediately adjacent to A < > A dimer sites (h_a: peak height at the damage site measured from the 3′ baseline) and that of the 5′ regions (h_b: height of the 5′, 500 bp upstream of the damage site, measured from the 3′ baseline) in the coding strand were quantified (Figure 5E). As h_b reached its maximum at ~1 h after UV in all cell types with a nearly identical profile (Figure 5E, dashed lines), this may reflect the "queueing" of multiple RNAPII molecules at the 5′ side of the T < > T dimer due to a "transcription traffic jam" right behind the RNAPII molecule that is stalled at the DNA lesion. The queue resolved swiftly in WT cells but persisted in TC-NER-deficient cells as well as in RPB1-K1268R cells, suggesting that RNAPIIo queueing and its resolution is associated with TC-NER activity and the processing of stalled RNAPIIo.

Gene-by-Gene Repair Profiles Identify Unrepaired Genic Features in RPB1-K1268R Cells

Analysis of SSI in individual genes exhibited a strong correlation between replicates both in WT and RPB1-K1268R cells at early time points (3–6 h) after UV irradiation in the entire genome (Figure 6A).This indicates that the TC-NER activity is not random but rather reflects a tight coordination between gene-by-gene transcription and repair. This correlation was reduced and stochastic events became more prominent at 12 h after UV, suggesting that random DNA repair by GG-NER dominates over TC-NER at this time point. Differential read coverage analysis identified genes that were left unrepaired (red dots in Figure 6A). These analyses were also performed in TC-NER-deficient cells (Figure S6A), which revealed an overlap in the sets of unrepaired genes between cell types (Figure 6B). While there was only 20% overlap between all conditions (WT-KR-ΔTCR), which reflects "common unrepaired genes" between WT and repair-deficient cell types (KR-ΔTCR), there was about 80% (KR-ΔTCR) overlap between unrepaired genes among the RPB1-K1268R (KR) and TC-NER-deficient (ΔTCR) cells. Within these overlapping genes, (Figure 6B), we analyzed common features, such as gene length (Figure 6C) and GC contents (Figure 6D), as well as RPB1 ChIP-seq read density, a proxy to gene expression level (Figure 6E) of the individual genes. The common unrepaired genes (WT-KR-ΔTCR, blue) as well as the overlapping genes between the KR and ΔTCR (green) cells were generally long in size and exhibited low-GC content and low-expression profiles, while genes only detected in the ΔTCR set (yellow) had no obvious characteristic features to distinguish them from "promptly repaired" genes (pink, 2,005 genes outside the Venn diagram in Figure 6B). Representative unrepaired genes in RPB1-K1268R cells are shown in Figure 6F.

We further performed a gene-enrichment analysis on the identified unrepaired genes in RPB1-K1268R that were repaired in WT cells. We detected a significant accumulation of unrepaired genes in the "cell-cycle" pathway (KEGG pathway ID hsa04110, $p = 5.60 \times 10^{-11}$; Figure S6B), such as genes encoding CDK-cyclin, ORC, and MCM (see *MCM3* repair profiles in Figure 5A) complexes, all of which positively regulate the cell-cycle progression. These cell-cycle genes are relatively long (median length: cell-cycle genes, 36 kb; other genes, 22 kb; $p = 7.69 \times 10^{-4}$, n = 9,836, Mann-Whitney U test), which likely explains this phenomenon. Our analyses suggest a possible cell-cycle delay and subsequent permanent cell-cycle arrest, resulting in cellular senescence in RPB1-K1268R cells in response to DNA damage.

Polr2a$^{K1268R/K1268R}$ / *Xpa*$^{-/-}$ Double-Mutant Mice Display Short Lifespan and a Premature Aging Phenotype

Having established a TC-NER-compromised cellular phenotype in RPB1-K1268R cells, we decided to examine the consequences of deficient RNAPIIo ubiquitination in a whole organism. We generated gene-edited mice with the RPB1-K1268R mutation. The RPB1-K1268R mutation was introduced into the *Polr2a* gene in C57BL/6 mouse by CRISPR/Cas9 (see STAR Methods). *Polr2a*$^{K1268R/K1268R\ (KR/KR)}$ homozygous knockin mice were generated after backcrosses of heterozygous founder mice and their inbreeding, which were born with expected Mendelian inheritance ratios. Neither the *Polr2a*$^{KR/KR}$ homozygous, nor the *Polr2a*$^{WT/KR}$ heterozygous mice displayed any remarkable abnormalities during the first year of farming. The mice are fertile and their weight and appearance are normal (Figure S7A; Table S4).

Indeed, in contrast to human CS individuals, TC-NER-deficient *Csa*$^{-/-}$ or *Csb*$^{-/-}$ mice do not show an obvious phenotype (van der Horst et al., 1997). A similar situation is observed in

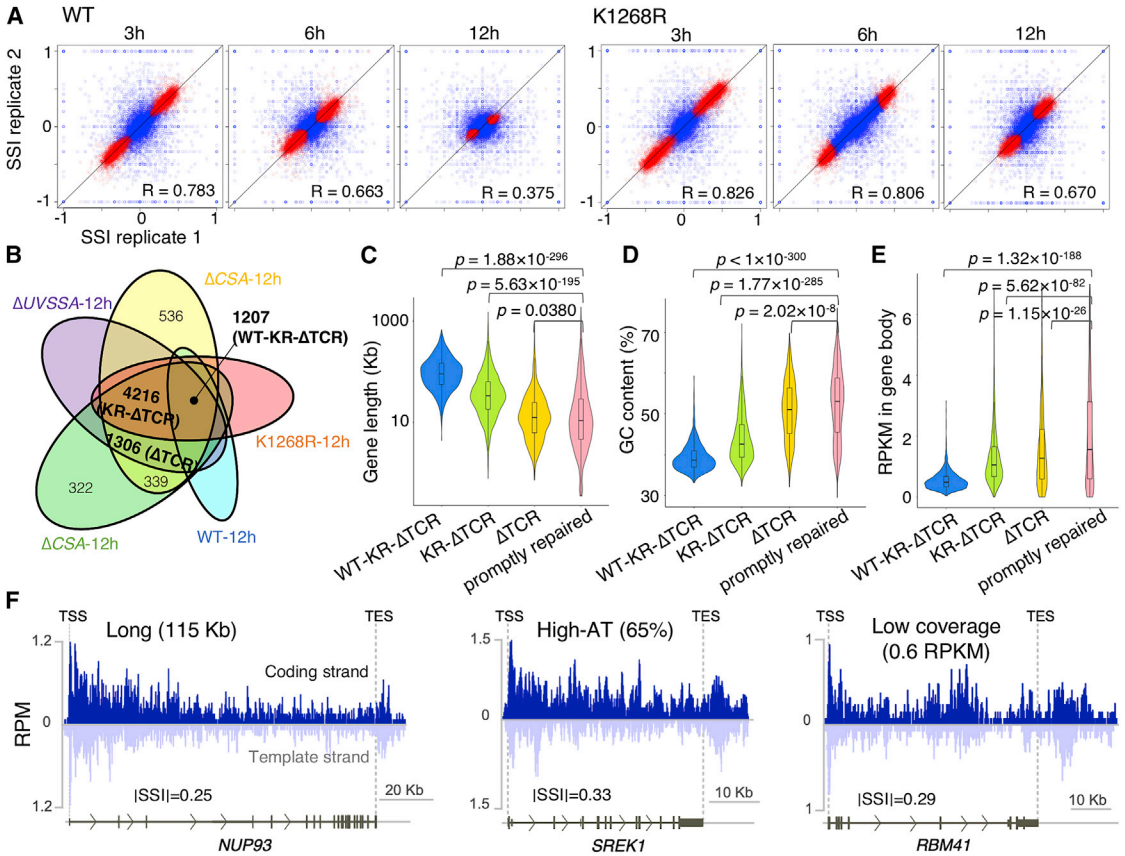

Figure 6. Gene-by-Gene Repair Profiles in RPB1-K1268R Mutant

(A) Strong gene-by-gene correlation of SSI (RPB1-Ser2, 3E10) between biological replicates in WT and RPB1-K1268R mutant HeLa cells. The genes presenting significantly high SSI are shown as red dots (Spearman's correlation coefficient was calculated for each pair). Those correlations between replicates of TC-NER-deficient cells are shown in Figure S6A.

(B) Venn diagram indicates the numbers of genes displaying significantly high SSI at 12 h after UV irradiation (representing the numbers of red dots in (A) (Figure S6A). About 80% of unrepaired genes are overlapping between RPB1-K1268R (KR) and TC-NER-deficient (ΔTCR) cells.

(C–E) Violin plots displaying distributions of gene lengths (C), GC contents (D), and read density in gene bodies (E) for individual genes in the gene sets determined in (B). p values were calculated with Mann-Whitney *U* test and were corrected by the Benjamini-Hochberg method.

(F) Strand-specific read distributions in representative unrepaired genes in RPB1-K1268R cells with profiles shown in (C)–(E).

See also Figure S6.

Fanconi anemia (FA) repair pathway (FANC)-deficient mice, which do not develop FA (Chen et al., 1996; Parmar et al., 2009). However, strong features of FA can be revealed by the genetic deletion of the aldehyde-catabolizing enzyme *Aldh2* in FANC-deficient mice (Langevin et al., 2011). Strikingly, clear CS-like features were reported in $Csb^{-/-}$ / $Xpa^{-/-}$ or $Csb^{-/-}$ / $Xpc^{-/-}$ double-mutant (DM) mice (Laposa et al., 2007; van der Pluijm et al., 2007), suggesting that increasing the DNA damage load due to GG-NER deficiency in $Csb^{-/-}$ or $Csa^{-/-}$ mutants now reveals a CS-like phenotype in mice.

In view of the above, we decided to generate $Polr2a^{KR/KR}$ / $Xpa^{-/-}$ DM mice to increase the likelihood of RNAPIIo colliding into DNA lesions during transcription and to reveal a potential CS-like phenotype. The DM mice displayed a remarkable growth retardation, low body weight, and prominent dwarfism (Figure 7A), although all the mice were born with expected Mendelian inheritance ratios. Littermates of these mice with other genotypes did not show any growth or neurological abnormalities (Figures 7A and S7B; Tables S5 and S6), similar to what was previously reported for $Xpa^{-/-}$ mice (Nakane et al., 1995). After 3 months, the DM mice gradually lost their body weights, which eventually resulted in death at the age of 5–6 months (Figure 7A; Table S6). Although daily observations confirmed the normal intake of food and water by the DM animals, their lifespan and condition did not improve. At 4–5 months of age, skeletal abnormalities, such as kyphosis and abnormal gait due to hindlimb dystonia were prominent in the DM mice, some of which also displayed depigmentation as well as cataracts, similar to human CS individuals (Calmels et al., 2018; Laugel, 2013) (Figures 7B and 7C; Table S6).

Loss of Motor Neurons in $Polr2a^{K1268R/K1268R}$ / $Xpa^{-/-}$ Double-Mutant Mice

The appearance of gait abnormalities and clamping hind limbs became evident after weaning in all DM animals, suggesting potential abnormalities in the central or peripheral nervous system.

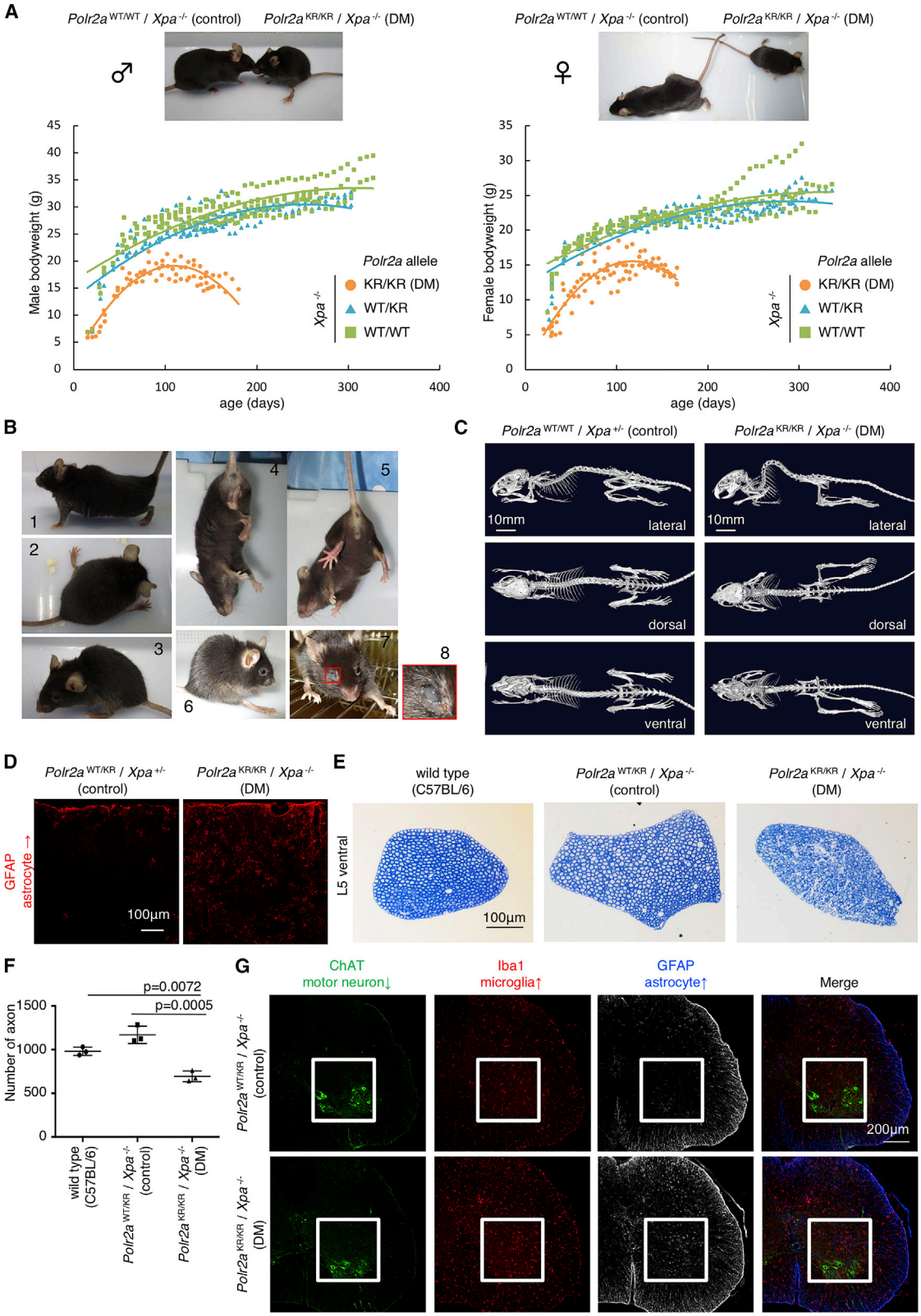

(legend on next page)

No obvious morphological abnormalities were apparent in the cerebrum and cerebellum of 4- to 6-month-old DM mice, except their small size in proportion to their body size. Interestingly, however, significant activation of astrocytes was observed in DM mice, implying the possibility of neuronal damage in the cerebral cortex (Figure 7D).

The gait abnormalities and dystonia in the DM mice could also be explained by motor neuron-specific abnormalities. To monitor potential progressive motor neuron loss, we quantified the number of axons in the spinal ventral roots from DM mice, which showed a terminal phenotype (>5 months). We observed a marked increase in the number of degenerating axons in the DM mice (Figure 7E), although the overall number of axons displayed a modest decrease compared to control mice (Figure 7F). Immunofluorescent stainings of spinal cords from DM mice also detected the loss of motor neurons (green), as well as activation of microglia (red) and astrocytes (white) (Figure 7G). These observations demonstrate that motor neuron degeneration in the DM animals is a late-onset progressive event, which is highly reminiscent of the progression in human CS individuals. The progressive neurodegenerative phenotype of the DM mice underscores the importance of RPB1-K1268 ubiquitination *in vivo* and suggests that these CS-like aging-related phenotypes are best explained by a deficiency in RNAPIIo processing and prolonged transcription arrests under a high load of endogenous DNA damage rather than a compromised DNA repair activity associated with TC-NER.

DISCUSSION

Although the ubiquitination of RNA polymerase IIo after UV irradiation in human cells has been known to occur for a considerable time (Bregman et al., 1996), the precise mechanisms and functions underlying this modification have remained unknown. Here, we report that a single DNA damage-induced ubiquitination site at RPB1-K1268 regulates both TC-NER and processing of DNA damage-stalled RNAPIIo on chromatin.

RNA Polymerase IIo Ubiquitination: Difference in Human versus Budding Yeast

DNA damage-induced ubiquitination of RNAPIIo is highly conserved from yeast to man. Elegant studies in the yeast *S. cerevisiae* have demonstrated that the ubiquitination of RNAPIIo by the Rsp5 and Def1 ubiquitin ligases is not required for TC-NER but rather acts as a last-resort pathway to remove and degrade RNAPIIo from DNA damage sites (Lommel et al., 2000; Somesh et al., 2005, 2007; Woudstra et al., 2002). Conversely, we show here that RPB1-K1268 ubiquitination in human cells does directly contribute to TC-NER (Figure 3F). While the RPB1-K1268 site and its surrounding amino acid residues are highly conserved in animals and plants, this region is less conserved in *S. cerevisiae* (Figure S1C), suggesting that the primary purpose of RNAPIIo ubiquitination between humans and budding yeast is different. In contrast, the RPB1-K1268 site is fairly conserved (*Rpb1*-K1252) in the fission yeast *S. pombe*, which in many ways shows more complex genomic features also found in vertebrate genomes. Interestingly, an *rpb1*-K1252R mutant in *S. pombe* showed increased sensitivity to the UV mimetic 4-NQO in an NER-deficient Δ*rhp14* (human *XPA* homolog) background (Figure S7C). This is reminiscent of our *Polr2a*^{K1268R} knockin mice, which displays a CS-like phenotype in an NER-deficient *Xpa*$^{-/-}$ background. These DNA repair-independent phenomena found in *S. pombe* and mice strongly suggest an evolutionarily conserved molecular mechanism, which underlies the resolution of transcription-damage collision by RNAPIIo ubiquitination at RPB1-K1268 (-K1252 in *S. pombe*) under a high load of DNA damage.

Players in RNA Polymerase IIo Ubiquitination in Human

The precise mechanisms involved in human RNAPIIo ubiquitination have been multitude and controversial. While earlier studies revealed that RNAPIIo ubiquitination is defective in cells deficient in CSA or CSB (Bregman et al., 1996; Ratner et al., 1998), more recent work by us (Nakazawa et al., 2012) and our current study also implicated UVSSA in this process, perhaps due to its association with deubiquitinase USP7 and the CSB/CSA

Figure 7. RPB1-K1268 Ubiquitination Protects against Neurodegeneration in Mice

(A) Body-weight distribution and growth curves of mice with the indicated genotypes. Representative control and *Polr2a*$^{K1268R/K1268R\ (KR/KR)}$ / *Xpa*$^{-/-}$ (DM) mice are shown at 144 days (males left, females right). Loss of body weight observed only in DM mice from 3 month after birth. Growth curves of mice with the WT *Xpa*$^{+/+}$ genotypes and the heterozygous *Xpa*$^{+/-}$ genotypes are shown in Figures S7A and S7B, respectively. See also Tables S4–S6. *Polr2a*$^{WT/WT}$ / *Xpa*$^{-/-}$ ♂ (n = 9); *Polr2a*$^{WT/KR}$ / *Xpa*$^{-/-}$ ♂ (n = 22); *Polr2a*$^{KR/KR}$ / *Xpa*$^{-/-}$ ♂ (n = 5); *Polr2a*$^{WT/WT}$ / *Xpa*$^{-/-}$ ♀ (n = 12); *Polr2a*$^{WT/KR}$ / *Xpa*$^{-/-}$ ♀ (n = 18); *Polr2a*$^{KR/KR}$ / *Xpa*$^{-/-}$ ♀ (n = 7).

(B) Representative premature aging phenotypes observed in DM mice. Kyphosis (1), gait abnormalities (2), and slimming (3) in a DM mouse (139 days). Hind-limb dystonia (clamping) (4) in a DM mouse (144 days) and a normal (5) *Polr2a*$^{WT/KR}$ / *Xpa*$^{-/-}$ littermate (144 days). Depigmentation (6) in a DM mouse (139 days). Cataract (7; 8, magnified view) in a DM mouse (153 days).

(C) Computed tomography images detected a severe kyphosis in a DM mouse (male, 180 days). A normal littermate control is shown (*Polr2a*$^{WT/WT}$ / *Xpa*$^{+/-}$ 180 days).

(D) Activation of astrocytes in the cerebral cortex was observed in DM mice (153 days) at an end stage compared to normal control (*Polr2a*$^{WT/\ KR}$ / *Xpa*$^{+/-}$, 153 days) by staining for GFAP (red).

(E) Representative images of toluidine blue-stained lumbar 5th ventral roots from a WT (C57BL/6), a control (*Polr2a*$^{WT/\ KR}$ / *Xpa*$^{-/-}$, 181 days), and a DM (163 days) mouse showing terminal phenotype. Degeneration of axons as well as decrease in the numbers of intact axons were observed.

(F) The axonal degeneration was observed in DM mice showing terminal phenotype. Average numbers of lumbar 5th motor axons are plotted (WT, C67BL/6, n = 3; control, *Polr2a*$^{WT/\ KR}$ / *Xpa*$^{-/-}$, n = 3; DM, n = 3). Data are presented as means (SD). p values were calculated with one-way ANOVA, followed by Tukey-Kramer post hoc tests.

(G) Loss of motor neurons as well as increase in the numbers of microglia and reactive astrocytes was observed in lumbar spinal cords (boxed regions) of a DM mouse at an end stage (166 days), compared to control *Polr2a*$^{WT/\ KR}$ / *Xpa*$^{-/-}$ (166 days) mice. Representative immunofluorescent images of lumbar spinal cord sections are shown stained for ChAT (green), Iba1 (red), GFAP (white).

See also Figure S7.

complex (Fei and Chen, 2012; Nakazawa et al., 2012; Schwertman et al., 2012; Zhang et al., 2012). Additionally, BRCA1/BARD1 (Kleiman et al., 2005; Starita et al., 2005), Elongin-Cullin complexes (Yasukawa et al., 2008), and the HECT E3 ligase NEDD4 (Anindya et al., 2007) have all been implicated in the UV-induced ubiquitination of human RNAPIIo.

Our findings reveal the near-complete loss of ubiquitination in RPB1-K1268R cells, suggesting that this lysine residue represents the main UV-induced ubiquitination site in RNAPIIo. The accompanying paper by Tufegdzic Vidakovic et al., 2020) also underscores the importance of this RPB1-K1268 ubiquitination for a proper transcription shutdown and recovery in response to UV irradiation. Notably, we observed severely reduced ubiquitination in Δ*CSA* cells, as well as complete loss of this modification after treatment with MLN4924, which suppresses NEDD8 conjugation to cullin-ring type E3 ligases (CRLs) causing their inactivation. These findings suggest that the $CRL4^{CSA}$ E3 ubiquitin ligase complex is a strong candidate to contributes to RPB1-K1268 ubiquitination.

RPB1-K1268 Ubiquitination Is Involved in TC-NER

The data presented in this study demonstrate that RPB1-K1268 ubiquitination is important for TC-NER. First, we show that RPB1-K1268R HeLa cells are very sensitive to UV irradiation and show an impaired recovery of RNA synthesis after UV. Second, strand-specific ChIP-seq analysis revealed that RPB1-K1268R cells showed significantly delayed removal of UV-induced DNA lesions from the transcribed strand of active genes. Third, molecular analysis revealed that the recruitment of the core-TFIIH complex to DNA damage-stalled RNAPIIo was significantly reduced in RPB1-K1268R cells, explaining the cellular TC-NER-compromised phenotype of these cells. This raises the question how RPB1-K1268 ubiquitination positions the TFIIH complex during TC-NER?

Our data support a model in which the association of CSB/CSA with DNA damage-stalled RNAPIIo is not affected by RPB1-K1268 ubiquitination. In fact, the CSB/CSA complex facilitates RPB1-K1268 ubiquitination upon its association with RNAPIIo, possibly together with other CRL ubiquitin ligases. The recruitment of UVSSA to RNAPIIo is fully dependent on CSB/CSA. Strikingly, the RPB1-UVSSA interaction is enhanced by RPB1-K1268 ubiquitination likely through the ubiquitin-binding VHS domain in UVSSA, which is most striking for mono-ubiquitinated UVSSA at K414. Although UVSSA initially associates with the TFIIH complex through interactions with the p62 subunit, UVSSA is eventually ubiquitinated at K414 to stimulate the displacement of p62 from UVSSA, possible in concert with other NER proteins. These parallel ubiquitination events of RPB1-K1268 and UVSSA-K414 facilitate the transfer of TFIIH to the DNA damage-stalled RNAPIIo (Figure 3F).

RPB1-K1268 Ubiquitination Has a Role in Damage-Stalled RNAPIIo Processing: Implications for Neurodegeneration

Our molecular analysis revealed that cells deficient in CSB, CSA, UVSSA, or RPB1-K1268 ubiquitination show a pronounced TC-NER deficiency. Strikingly, however, only defects in the *CSA* or *CSB* genes in humans cause the neurodegenerative disorder Cockayne syndrome (CS), which is characterized by dysmyelination, progressive loss of neurons, severe developmental abnormalities, and premature aging. Conversely, defects in *UVSSA* cause the mild UV-sensitive syndrome ($UV^{S}S$) without devastating features seen in CS, implying that CS is not caused by compromised TC-NER (Nakazawa et al., 2012).

Our current findings shed light on the molecular pathogenesis of CS by revealing that $Polr2a^{K1268R}$ mice deficient in the DNA damage-induced ubiquitination of RNAPIIo show pronounced dwarfism, growth retardation, neurodegeneration, and short lifespan reminiscent of CS. This phenotype only became prominent in the DNA repair-compromised $Xpa^{-/-}$ background, which lacks both GG-NER and TC-NER activity but displays no obvious characteristics including neurological abnormalities, although $Xpa^{-/-}$ mice are skin cancer predisposed after UV irradiation (Nakane et al., 1995). This is in line with the absence of CS-like neurodegeneration in human XP-A individuals (Brooks, 2008). Importantly, our findings strongly argue that CS-like features are not caused by defective TC-NER. Indeed, neurodegeneration in $Csb^{-/-}$ mice was also only observed in an NER-compromised background, such as $Xpa^{-/-}$ or $Xpc^{-/-}$ mice (Laposa et al., 2007; van der Pluijm et al., 2007), suggesting that this phenotype, in mice, is only unmasked by an excess of unrepaired endogenous DNA lesions ordinarily dealt with by NER. We have noted previously that *CSA* or *CSB*-deficient primary fibroblasts fail to degrade RNAPIIo after UV irradiation, while *UVSSA*-deficient cells showed swift degradation (Nakazawa et al., 2012). This has led to a hypothesis in which a deficiency in RNAPIIo processing and prolonged transcription arrests in response to DNA damage rather than a compromised TC-NER activity underlies the CS-like neurodegenerative phenotype (Nakazawa et al., 2012). The CS-like phenotype of the $Polr2a^{K1268R}$ mice fully supports this model. In addition to the intrinsic TC-NER deficiency, a failure to ubiquitinate RPB1-K1268 leads to a non-displaceable RNAPIIo molecule, which blocks accessibility of the DNA lesions to alternative repair pathways, like GG-NER, and causes prolonged transcription arrests. Indeed, aldehydes and cyclopurines are likely endogenous DNA lesions in the brain that block RNAPIIo progression and may strongly contribute to the CS phenotype in case RNAPIIo processing is compromised. This model provides an explanation for the different clinical features associated with TC-NER-deficiency disorders. Similarly, defects in processing of RNAPII at various types of DNA damage may contribute to develop neurodegenerative phenotype shared among genome instability disorders.

STAR★METHODS

Detailed methods are provided in the online version of this paper and include the following:

- KEY RESOURCES TABLE
- LEAD CONTACT AND MATERIALS AVAILABILITY
- EXPERIMENTAL MODEL AND SUBJECT DETAILS
  - Human cell lines and culture
  - Mice
  - S. pombe

SUPPLEMENTAL INFORMATION

Supplemental Information can be found onl2ine at https://doi.org/10.1016/j.cell.2020.02.010.

ACKNOWLEDGMENTS

This paper is dedicated to the memory of a wonderful lady, Amy Garton-Hughes, who made a huge difference in the lives of Cockayne syndrome children. We are grateful to Drs. Alan Lehman and Chikahide Masutani for their helpful comments and discussions on the manuscript. We are grateful to Dr. Masato Kanemaki for his advice on the CRISPR/Cas9-based gene targeting experiments. Bioinformatics data processing was partially performed using the super-computing resource provided by Human Genome Center, the Institute of Medical Science, the University of Tokyo. This work was supported by the Special Coordination Funds for Rare and Intractable Diseases from Japan Agency for Medical Research and Development (AMED) (JP19ek0109281, JP19ek0109229, and JP19ek0109301), Grants in Aid for Scientific Research KAKENHI (JP15H02654 and JP17H00783) from the Japan Society for the Promotion of Science, a Science Research Grant from the Uehara Memorial Foundation, a grant from the Daiko Foundation, and a medical research grant from the Takeda Science Foundation to T.O.; KAKENHI (JP17H01877) and a medical research grant from Takeda Science Foundation to Y.N.; TBRF Postdoctoral Fellowship for Asian Researchers in Japan from The Tokyo Biochemical Research Foundation (TBRF) to C.G. and T.O.; and an LUMC research fellowship and an NWO-VIDI grant (016.161.320) to M.S.L.

AUTHOR CONTRIBUTIONS

T.O. designed the study and experiments. Y.N., Y.O., D.V.d.H., C.G., Y.D., M.I., Y. He, M.S., K.K., N.J., S.H., M.S.L, and T.O. performed molecular and cell biological experiments. Y. Hara, and T.O. performed bioinformatics analyses. Y.O., O.K., C.G., Y. He, M.S., Y.K., Y.M., M.T., A.S., T.M., K.Y., and T.O. performed animal studies. N.M and S.N. contributed materials. N.M., T.S., A.M., K.O., S.N., T.M., K.Y., M.S.L., and T.O. coordinated the study. M.S.L. and T.O. wrote the manuscript. All authors commented on the manuscript.

DECLARATION OF INTERESTS

The authors declare no competing interests.

Received: July 22, 2019
Revised: December 16, 2019
Accepted: February 4, 2020
Published: March 5, 2020

REFERENCES

Aboussekhra, A., Biggerstaff, M., Shivji, M.K., Vilpo, J.A., Moncollin, V., Podust, V.N., Protić, M., Hübscher, U., Egly, J.M., and Wood, R.D. (1995). Mammalian DNA nucleotide excision repair reconstituted with purified protein components. Cell *80*, 859–868.

Anindya, R., Aygün, O., and Svejstrup, J.Q. (2007). Damage-induced ubiquitylation of human RNA polymerase II by the ubiquitin ligase Nedd4, but not Cockayne syndrome proteins or BRCA1. Mol. Cell *28*, 386–397.

Bähler, J., Wu, J.Q., Longtine, M.S., Shah, N.G., McKenzie, A., 3rd, Steever, A.B., Wach, A., Philippsen, P., and Pringle, J.R. (1998). Heterologous modules for efficient and versatile PCR-based gene targeting in Schizosaccharomyces pombe. Yeast *14*, 943–951.

Bolger, A.M., Lohse, M., and Usadel, B. (2014). Trimmomatic: a flexible trimmer for Illumina sequence data. Bioinformatics *30*, 2114–2120.

Bregman, D.B., Halaban, R., van Gool, A.J., Henning, K.A., Friedberg, E.C., and Warren, S.L. (1996). UV-induced ubiquitination of RNA polymerase II: a novel modification deficient in Cockayne syndrome cells. Proc. Natl. Acad. Sci. USA *93*, 11586–11590.

Brookes, E., de Santiago, I., Hebenstreit, D., Morris, K.J., Carroll, T., Xie, S.Q., Stock, J.K., Heidemann, M., Eick, D., Nozaki, N., et al. (2012). Polycomb associates genome-wide with a specific RNA polymerase II variant, and regulates metabolic genes in ESCs. Cell Stem Cell *10*, 157–170.

Brooks, P.J. (2008). The 8,5′-cyclopurine-2′-deoxynucleosides: candidate neurodegenerative DNA lesions in xeroderma pigmentosum, and unique probes of transcription and nucleotide excision repair. DNA Repair (Amst.) *7*, 1168–1179.

Brueckner, F., Hennecke, U., Carell, T., and Cramer, P. (2007). CPD damage recognition by transcribing RNA polymerase II. Science *315*, 859–862.

Calmels, N., Botta, E., Jia, N., Fawcett, H., Nardo, T., Nakazawa, Y., Lanzafame, M., Moriwaki, S., Sugita, K., Kubota, M., et al. (2018). Functional and clinical relevance of novel mutations in a large cohort of patients with Cockayne syndrome. J. Med. Genet. *55*, 329–343.

Chen, M., Tomkins, D.J., Auerbach, W., McKerlie, C., Youssoufian, H., Liu, L., Gan, O., Carreau, M., Auerbach, A., Groves, T., et al. (1996). Inactivation of Fac in mice produces inducible chromosomal instability and reduced fertility reminiscent of Fanconi anaemia. Nat. Genet. *12*, 448–451.

Elia, A.E., Boardman, A.P., Wang, D.C., Huttlin, E.L., Everley, R.A., Dephoure, N., Zhou, C., Koren, I., Gygi, S.P., and Elledge, S.J. (2015). Quantitative Proteomic Atlas of Ubiquitination and Acetylation in the DNA Damage Response. Mol. Cell *59*, 867–881.

Fedorov, A., Beichel, R., Kalpathy-Cramer, J., Finet, J., Fillion-Robin, J.-C., Pujol, S., Bauer, C., Jennings, D., Fennessy, F., Sonka, M., et al. (2012). 3D

Slicer as an image computing platform for the Quantitative Imaging Network. Magn. Reson. Imaging *30*, 1323–1341.

Fei, J., and Chen, J. (2012). KIAA1530 protein is recruited by Cockayne syndrome complementation group protein A (CSA) to participate in transcription-coupled repair (TCR). J. Biol. Chem. *287*, 35118–35126.

Friedberg, E.C., Walker, G.C., Siede, W., Wood, R.D., Schultz, R.A., and Ellenberger, T. (2005). DNA Repair and Mutagenesis, Second Edition (ASM Press).

Gregersen, L.H., and Svejstrup, J.Q. (2018). The Cellular Response to Transcription-Blocking DNA Damage. Trends Biochem. Sci. *43*, 327–341.

Haeussler, M., Schönig, K., Eckert, H., Eschstruth, A., Mianné, J., Renaud, J.B., Schneider-Maunoury, S., Shkumatava, A., Teboul, L., Kent, J., et al. (2016). Evaluation of off-target and on-target scoring algorithms and integration into the guide RNA selection tool CRISPOR. Genome Biol. *17*, 148.

Hanawalt, P.C., and Spivak, G. (2008). Transcription-coupled DNA repair: two decades of progress and surprises. Nat. Rev. Mol. Cell Biol. *9*, 958–970.

He, Y., Yan, C., Fang, J., Inouye, C., Tjian, R., Ivanov, I., and Nogales, E. (2016). Near-atomic resolution visualization of human transcription promoter opening. Nature *533*, 359–365.

Higa, M., Tanaka, K., and Saijo, M. (2018). Inhibition of UVSSA ubiquitination suppresses transcription-coupled nucleotide excision repair deficiency caused by dissociation from USP7. FEBS J. *285*, 965–976.

Jackson, S.P., and Bartek, J. (2009). The DNA-damage response in human biology and disease. Nature *461*, 1071–1078.

Jia, N., Nakazawa, Y., Guo, C., Shimada, M., Sethi, M., Takahashi, Y., Ueda, H., Nagayama, Y., and Ogi, T. (2015). A rapid, comprehensive system for assaying DNA repair activity and cytotoxic effects of DNA-damaging reagents. Nat. Protoc. *10*, 12–24.

Kanehisa, M., and Goto, S. (2000). KEGG: kyoto encyclopedia of genes and genomes. Nucleic Acids Res. *28*, 27–30.

Kashiyama, K., Nakazawa, Y., Pilz, D.T., Guo, C., Shimada, M., Sasaki, K., Fawcett, H., Wing, J.F., Lewin, S.O., Carr, L., et al. (2013). Malfunction of nuclease ERCC1-XPF results in diverse clinical manifestations and causes Cockayne syndrome, xeroderma pigmentosum, and Fanconi anemia. Am. J. Hum. Genet. *92*, 807–819.

Kleiman, F.E., Wu-Baer, F., Fonseca, D., Kaneko, S., Baer, R., and Manley, J.L. (2005). BRCA1/BARD1 inhibition of mRNA 3′ processing involves targeted degradation of RNA polymerase II. Genes Dev. *19*, 1227–1237.

Langevin, F., Crossan, G.P., Rosado, I.V., Arends, M.J., and Patel, K.J. (2011). Fancd2 counteracts the toxic effects of naturally produced aldehydes in mice. Nature *475*, 53–58.

Laposa, R.R., Huang, E.J., and Cleaver, J.E. (2007). Increased apoptosis, p53 up-regulation, and cerebellar neuronal degeneration in repair-deficient Cockayne syndrome mice. Proc. Natl. Acad. Sci. USA *104*, 1389–1394.

Laugel, V. (2013). Cockayne syndrome: the expanding clinical and mutational spectrum. Mech. Ageing Dev. *134*, 161–170.

Li, H. (2013). Aligning sequence reads, clone sequences and assembly contigs with BWA-MEM. arXiv, arXiv:1303.3997.

Li, H., Handsaker, B., Wysoker, A., Fennell, T., Ruan, J., Homer, N., Marth, G., Abecasis, G., and Durbin, R.; 1000 Genome Project Data Processing Subgroup (2009). The Sequence Alignment/Map format and SAMtools. Bioinformatics *25*, 2078–2079.

Limsirichaikul, S., Niimi, A., Fawcett, H., Lehmann, A., Yamashita, S., and Ogi, T. (2009). A rapid non-radioactive technique for measurement of repair synthesis in primary human fibroblasts by incorporation of ethynyl deoxyuridine (EdU). Nucleic Acids Res. *37*, e31.

Ljungman, M., and Zhang, F. (1996). Blockage of RNA polymerase as a possible trigger for u.v. light-induced apoptosis. Oncogene *13*, 823–831.

Lommel, L., Bucheli, M.E., and Sweder, K.S. (2000). Transcription-coupled repair in yeast is independent from ubiquitylation of RNA pol II: implications for Cockayne's syndrome. Proc. Natl. Acad. Sci. USA *97*, 9088–9092.

Marteijn, J.A., Lans, H., Vermeulen, W., and Hoeijmakers, J.H. (2014). Understanding nucleotide excision repair and its roles in cancer and ageing. Nat. Rev. Mol. Cell Biol. *15*, 465–481.

Mayer, A., Landry, H.M., and Churchman, L.S. (2017). Pause & go: from the discovery of RNA polymerase pausing to its functional implications. Curr. Opin. Cell Biol. *46*, 72–80.

McKenna, A., Hanna, M., Banks, E., Sivachenko, A., Cibulskis, K., Kernytsky, A., Garimella, K., Altshuler, D., Gabriel, S., Daly, M., and DePristo, M.A. (2010). The Genome Analysis Toolkit: a MapReduce framework for analyzing next-generation DNA sequencing data. Genome Res. *20*, 1297–1303.

Menoni, H., Wienholz, F., Theil, A.F., Janssens, R.C., Lans, H., Campalans, A., Radicella, J.P., Marteijn, J.A., and Vermeulen, W. (2018). The transcription-coupled DNA repair-initiating protein CSB promotes XRCC1 recruitment to oxidative DNA damage. Nucleic Acids Res. *46*, 7747–7756.

Moreno, S., Klar, A., and Nurse, P. (1991). Molecular genetic analysis of fission yeast Schizosaccharomyces pombe. Methods Enzymol. *194*, 795–823.

Naito, Y., Hino, K., Bono, H., and Ui-Tei, K. (2015). CRISPRdirect: software for designing CRISPR/Cas guide RNA with reduced off-target sites. Bioinformatics *31*, 1120–1123.

Nakane, H., Takeuchi, S., Yuba, S., Saijo, M., Nakatsu, Y., Murai, H., Nakatsuru, Y., Ishikawa, T., Hirota, S., Kitamura, Y., et al. (1995). High incidence of ultraviolet-B-or chemical-carcinogen-induced skin tumours in mice lacking the xeroderma pigmentosum group A gene. Nature *377*, 165–168.

Nakazawa, Y., Yamashita, S., Lehmann, A.R., and Ogi, T. (2010). A semi-automated non-radioactive system for measuring recovery of RNA synthesis and unscheduled DNA synthesis using ethynyluracil derivatives. DNA Repair (Amst.) *9*, 506–516.

Nakazawa, Y., Sasaki, K., Mitsutake, N., Matsuse, M., Shimada, M., Nardo, T., Takahashi, Y., Ohyama, K., Ito, K., Mishima, H., et al. (2012). Mutations in UVSSA cause UV-sensitive syndrome and impair RNA polymerase IIo processing in transcription-coupled nucleotide-excision repair. Nat. Genet. *44*, 586–592.

Nouspikel, T. (2011). Multiple roles of ubiquitination in the control of nucleotide excision repair. Mech. Ageing Dev. *132*, 355–365.

Odawara, J., Harada, A., Yoshimi, T., Maehara, K., Tachibana, T., Okada, S., Akashi, K., and Ohkawa, Y. (2011). The classification of mRNA expression levels by the phosphorylation state of RNAPII CTD based on a combined genome-wide approach. BMC Genomics *12*, 516.

Okuda, M., Nakazawa, Y., Guo, C., Ogi, T., and Nishimura, Y. (2017). Common TFIIH recruitment mechanism in global genome and transcription-coupled repair subpathways. Nucleic Acids Res. *45*, 13043–13055.

Parmar, K., D'Andrea, A., and Niedernhofer, L.J. (2009). Mouse models of Fanconi anemia. Mutat. Res. *668*, 133–140.

Paulsen, M.T., Veloso, A., Prasad, J., Bedi, K., Ljungman, E.A., Magnuson, B., Wilson, T.E., and Ljungman, M. (2014). Use of Bru-Seq and BruChase-Seq for genome-wide assessment of the synthesis and stability of RNA. Methods *67*, 45–54.

Quinlan, A.R., and Hall, I.M. (2010). BEDTools: a flexible suite of utilities for comparing genomic features. Bioinformatics *26*, 841–842.

Rahl, P.B., Lin, C.Y., Seila, A.C., Flynn, R.A., McCuine, S., Burge, C.B., Sharp, P.A., and Young, R.A. (2010). c-Myc regulates transcriptional pause release. Cell *141*, 432–445.

Ramírez, F., Dündar, F., Diehl, S., Grüning, B.A., and Manke, T. (2014). deepTools: a flexible platform for exploring deep-sequencing data. Nucleic Acids Res. *42*, W187–W191.

Ran, F.A., Hsu, P.D., Wright, J., Agarwala, V., Scott, D.A., and Zhang, F. (2013). Genome engineering using the CRISPR-Cas9 system. Nat. Protoc. *8*, 2281–2308.

Ratner, J.N., Balasubramanian, B., Corden, J., Warren, S.L., and Bregman, D.B. (1998). Ultraviolet radiation-induced ubiquitination and proteasomal degradation of the large subunit of RNA polymerase II. Implications for transcription-coupled DNA repair. J. Biol. Chem. *273*, 5184–5189.

Raudvere, U., Kolberg, L., Kuzmin, I., Arak, T., Adler, P., Peterson, H., and Vilo, J. (2019). g:Profiler: a web server for functional enrichment analysis and conversions of gene lists (2019 update). Nucleic Acids Res. *47* (W1), W191–W198.

Reid-Bayliss, K.S., Arron, S.T., Loeb, L.A., Bezrookove, V., and Cleaver, J.E. (2016). Why Cockayne syndrome patients do not get cancer despite their DNA repair deficiency. Proc. Natl. Acad. Sci. USA *113*, 10151–10156.

Robinson, M.D., McCarthy, D.J., and Smyth, G.K. (2010). edgeR: a Bioconductor package for differential expression analysis of digital gene expression data. Bioinformatics *26*, 139–140.

Schwertman, P., Lagarou, A., Dekkers, D.H., Raams, A., van der Hoek, A.C., Laffeber, C., Hoeijmakers, J.H., Demmers, J.A., Fousteri, M., Vermeulen, W., and Marteijn, J.A. (2012). UV-sensitive syndrome protein UVSSA recruits USP7 to regulate transcription-coupled repair. Nat. Genet. *44*, 598–602.

Shen, L., Shao, N., Liu, X., and Nestler, E. (2014). ngs.plot: Quick mining and visualization of next-generation sequencing data by integrating genomic databases. BMC Genomics *15*, 284.

Somesh, B.P., Reid, J., Liu, W.F., Søgaard, T.M., Erdjument-Bromage, H., Tempst, P., and Svejstrup, J.Q. (2005). Multiple mechanisms confining RNA polymerase II ubiquitylation to polymerases undergoing transcriptional arrest. Cell *121*, 913–923.

Somesh, B.P., Sigurdsson, S., Saeki, H., Erdjument-Bromage, H., Tempst, P., and Svejstrup, J.Q. (2007). Communication between distant sites in RNA polymerase II through ubiquitylation factors and the polymerase CTD. Cell *129*, 57–68.

Soucy, T.A., Smith, P.G., Milhollen, M.A., Berger, A.J., Gavin, J.M., Adhikari, S., Brownell, J.E., Burke, K.E., Cardin, D.P., Critchley, S., et al. (2009). An inhibitor of NEDD8-activating enzyme as a new approach to treat cancer. Nature *458*, 732–736.

Starita, L.M., Horwitz, A.A., Keogh, M.C., Ishioka, C., Parvin, J.D., and Chiba, N. (2005). BRCA1/BARD1 ubiquitinate phosphorylated RNA polymerase II. J. Biol. Chem. *280*, 24498–24505.

Storey, J.D., and Tibshirani, R. (2003). Statistical significance for genomewide studies. Proc. Natl. Acad. Sci. USA *100*, 9440–9445.

Sugaya, K., Vigneron, M., and Cook, P.R. (2000). Mammalian cell lines expressing functional RNA polymerase II tagged with the green fluorescent protein. J. Cell Sci. *113*, 2679–2683.

Thorvaldsdóttir, H., Robinson, J.T., and Mesirov, J.P. (2013). Integrative Genomics Viewer (IGV): high-performance genomics data visualization and exploration. Brief. Bioinform. *14*, 178–192.

Tischler, G., and Leonard, S. (2014). biobambam: tools for read pair collation based algorithms on BAM files. Source Code Biol. Med. *9*, 13. Published online June 20, 2014. https://doi.org/10.1186/1751-0473-9-13.

Tufegdzic Vidakovic, A., Mitter, R., Kelly, G.P., Neumann, M., Harreman, M., Rodriguez Martinez, M., Herlihy, A., Weems, J.C., Boeing, S., Encheva, V., et al. (2020). Regulation of the RNAPII pool is integral to the DNA damage response. Cell *180*. Published online March 5, 2020. https://doi.org/10.1016/j.cell.2020.02.009.

van der Horst, G.T., van Steeg, H., Berg, R.J., van Gool, A.J., de Wit, J., Weeda, G., Morreau, H., Beems, R.B., van Kreijl, C.F., de Gruijl, F.R., et al. (1997). Defective transcription-coupled repair in Cockayne syndrome B mice is associated with skin cancer predisposition. Cell *89*, 425–435.

van der Pluijm, I., Garinis, G.A., Brandt, R.M., Gorgels, T.G., Wijnhoven, S.W., Diderich, K.E., de Wit, J., Mitchell, J.R., van Oostrom, C., Beems, R., et al. (2007). Impaired genome maintenance suppresses the growth hormone–insulin-like growth factor 1 axis in mice with Cockayne syndrome. PLoS Biol. *5*, e2.

van der Weegen, Y., Berman, H.G., Mevissen, T.E.T., Apelt, K., González-Prieto, R., Heilbrun, E., Vertegaal, A.C.O., van den Heuvel, D., Walter, J.C., Adar, S., and Luijsterburg, M.S. (2019). The sequential and cooperative action of CSB, CSA and UVSSA targets the TFIIH complex to DNA damage-stalled RNA polymerase II. bioRxiv. https://doi.org/10.1101/707216v1.

Wang, Y., Chakravarty, P., Ranes, M., Kelly, G., Brooks, P.J., Neilan, E., Stewart, A., Schiavo, G., and Svejstrup, J.Q. (2014). Dysregulation of gene expression as a cause of Cockayne syndrome neurological disease. Proc. Natl. Acad. Sci. USA *111*, 14454–14459.

Watson, A.T., Garcia, V., Bone, N., Carr, A.M., and Armstrong, J. (2008). Gene tagging and gene replacement using recombinase-mediated cassette exchange in Schizosaccharomyces pombe. Gene *407*, 63–74.

Woudstra, E.C., Gilbert, C., Fellows, J., Jansen, L., Brouwer, J., Erdjument-Bromage, H., Tempst, P., and Svejstrup, J.Q. (2002). A Rad26-Def1 complex coordinates repair and RNA pol II proteolysis in response to DNA damage. Nature *415*, 929–933.

Xu, J., Lahiri, I., Wang, W., Wier, A., Cianfrocco, M.A., Chong, J., Hare, A.A., Dervan, P.B., DiMaio, F., Leschziner, A.E., and Wang, D. (2017). Structural basis for the initiation of eukaryotic transcription-coupled DNA repair. Nature *551*, 653–657.

Yamaizumi, M., and Sugano, T. (1994). U.v.-induced nuclear accumulation of p53 is evoked through DNA damage of actively transcribed genes independent of the cell cycle. Oncogene *9*, 2775–2784.

Yasukawa, T., Kamura, T., Kitajima, S., Conaway, R.C., Conaway, J.W., and Aso, T. (2008). Mammalian Elongin A complex mediates DNA-damage-induced ubiquitylation and degradation of Rpb1. EMBO J. *27*, 3256–3266.

Zhang, X., Horibata, K., Saijo, M., Ishigami, C., Ukai, A., Kanno, S., Tahara, H., Neilan, E.G., Honma, M., Nohmi, T., et al. (2012). Mutations in UVSSA cause UV-sensitive syndrome and destabilize ERCC6 in transcription-coupled DNA repair. Nat. Genet. *44*, 593–597.

STAR★METHODS

KEY RESOURCES TABLE

REAGENT or RESOURCE	SOURCE	IDENTIFIER
Antibodies		
rat anti-RPB1-phospho-Ser2-CTD (RPB1-Ser2), clone 3E10	Millipore	Cat# 04-1571; RRID: AB_11212363
rat anti-RPB1-phospho-Ser5-CTD (RPB1-Ser5), clone 3E8	Millipore	Cat# 04-1572; RRID: AB_10615822
rabbit anti-RPB1-phospho-Ser2-CTD (RPB1-Ser2)	Abcam	Cat# ab5095; RRID: AB_304749
rabbit anti-RNA Polymerase II	Bethyl Laboratories	Cat# A304-405A; RRID: AB_2620600
mouse anti- mono-, and poly-ubiquitin, clone FK2	ENZO Life Sciences	Cat# BML-PW8810; RRID: AB_10541840
mouse anti-ubiquitin, clone P4D1	Santa Cruz	Cat# sc-8017; RRID: AB_2762364
rabbit anti-K48-linkage specific polyubiquitin, clone Apu2	Millipore	Cat# 05-1307; RRID: AB_1587578
mouse anti-K63-linkage specific polyubiquitin, clone HWA4C4	eBioscience	Cat# 14-6077-80; RRID: AB_1257214
rabbit anti-SMC3	Bethyl laboratories	Cat# A300-060A; RRID: AB_67579
rabbit anti-Cul4A	Bethyl Laboratories	Cat# A300-739A; RRID: AB_533380
mouse anti-PCNA, clone PC-10	NeoMarkers	Cat# MS-106-P0; RRID: AB_64276
mouse anti-GFP, clone B-2	Santa Cruz	Cat# sc-9996; RRID: AB_627695
rabbit anti-RAD21 (D213)	Cell Signaling Technologies	Cat# 4321; RRID: AB_1904106
mouse anti-TFIIH p62/GTF2H1, clone G-10	Santa Cruz	Cat# sc-48431; RRID: AB_2247962
mouse anti-TFIIH p89/XPB, clone G-10	Santa Cruz	Cat# sc-271500; RRID: AB_10649033
mouse anti-cdk7 (MO1)	MBL	Cat# K0068-3; RRID: AB_591059
mouse anti-CSB/ERCC6, clone 553C5a	Bio Matrix Research	Cat# BMR00638
rabbit anti-CSA/ERCC8, clone EPR9237	Abcam	Cat# ab137033; RRID: AB_2783825
mouse anti-cdk9, clone D-7	Santa Cruz	Cat# sc-13130; RRID: AB_627245
mouse anti-Cyclin T1, clone E-3	Santa Cruz	Cat# sc-271348; RRID: AB_10608086
mouse anti-SPT5, clone D-3	Santa Cruz	Cat# sc-133217; RRID: AB_2196394
mouse anti-UVSSA	Abnova	Cat# H00057654-B01P; RRID: AB_11016566
HRP-conjugated mouse anti-myc-tag	MBL	Cat# M192-7
rabbit anti-V5-tag	MBL	Cat# PM003; RRID: AB_592941
goat anti-Choline Acetyltransferase (ChAT)	Millipore	Cat# AB144P; RRID: AB_2079751
rabbit anti-Iba1	Wako	Cat# 019-19741; RRID: AB_839504
mouse anti-glial fibrillary acidic protein (GFAP), clone G-A-5	Sigma	Cat# G3893; RRID: AB_477010
Anti-mouse IgG, HRP-linked	Cell Signaling Technologies	Cat# 7076; RRID: AB_330924
Anti-rabbit IgG, HRP-linked	Cell Signaling Technologies	Cat# 7074; RRID: AB_2099233
Anti-rat IgG, HRP-linked	Cell Signaling Technologies	Cat# 7077; RRID: AB_10694715
Goat anti-Mouse IgG (H+L) Highly Cross-Adsorbed Secondary Antibody, Alexa Fluor 546	Thermo Fisher Scientific	Cat# A11030; RRID: AB_144695
Cy3 AffiniPure Donkey Anti-Rabbit IgG (H+L)	Jackson Immuno Research laboratories	Cat# 711-165-152; RRID: AB_2307443

(*Continued on next page*)

Continued

REAGENT or RESOURCE	SOURCE	IDENTIFIER
Alexa Fluor 647 AffiniPure Donkey Anti-Mouse IgG (H+L)	Jackson Immuno Research laboratories	Cat# 715-605-150; RRID: AB_2340862
Donkey anti-Goat IgG (H+L) Cross-Adsorbed Secondary Antibody, Alexa Fluor 488	Thermo Fisher Scientific	Cat# A11055; RRID: AB_2534102
Bacterial and Virus Strains		
pLenti-6-*UVSSA*-V5 (lentivirus particle)	Nakazawa et al., (2012)	N/A
pLenti-6-*UVSSA*-K414R-V5 (lentivirus particle)	This study	N/A
pLenti-6-*UVSSA*-F408A-V5 (lentivirus particle)	Okuda et al., (2017)	N/A
pLenti-6-*UVSSA*-V411A-V5 (lentivirus particle)	Okuda et al., (2017)	N/A
Chemicals, Peptides, and Recombinant Proteins		
D-MEM (High Glucose) with L-Glutamine, Phenol Red and Sodium Pyruvate (DMEM)	Wako	043-30085
fetal bovine serum (FBS)	Thermo Fisher Scientific (GIBCO)	10437-028
Penicillin-Streptomycin Solution (× 100)	Wako	168-23191
D-PBS (PBS-)	Wako	045-29795
0.05 w/v% Trypsin-0.53 mmol/L EDTA 4Na Solution with Phenol Red (Trypsin/EDTA)	Wako	204-16935
recombinant Cas9, Alt-R S.p. Cas9 Nuclease 3NLS	IDT	1074181
KSOM medium	ARK Resource	KSOM
Opti-MEM I Reduced Serum Medium	Thermo Fisher Scientific	31985062
sevoflurane	Mylan	1900AMX00269
isoflurane	Mylan	22700AMX00134
standard certified diet pellet (MF)	Oriental Yeast	MF
Lipofectamine 2000 Transfection Reagent	Thermo Fisher Scientific	11668019
Puromycin Dihydrochloride from Streptomyces alboniger (Puromycin)	Nacalai	29455-54
DMEM for SILAC	Thermo Fisher Scientific	88364
Fetal Bovine Serum dialyzed (FBS) for SILAC	SAFC Biosciences	12117C
L-Arginine-HCl for SILAC	Thermo Fisher Scientific	89989
L-Lysine-2HCl for SILAC	Thermo Fisher Scientific	89987
L-Arginine-^{13}C6,^{15}N4 Hydrochloride for SILAC	Wako	010-24041
L-Lysine-^{13}C6,^{15}N2 Monohydrochloride for SILAC	Wako	123-06081
1,4-dithiothreitol	Thermo Fisher Scientific	R0861
iodoacetamide	Millipore	144-48-9
Lysyl Endopeptidase, Mass Spectrometry Grade, Lys-C	Wako	125-05061
Pierce Trypsin Protease, MS Grade	Thermo Fisher Scientific	90059
Igepal Ca-630 Non-Ionic Detergent (NP-40)	Wako	198596
cOmplete, EDTA-free Protease Inhibitor Cocktail Tablets	Roche	5056489001
Benzonase Nuclease	Millipore	70664
dimethyl sulfoxide (DMSO)	Sigma	D5879
MLN4924	ChemScene	CS-0348

(*Continued on next page*)

Continued

REAGENT or RESOURCE	SOURCE	IDENTIFIER
5-ethynyluridine (EU)	Thermo Fisher Scientific	E10345
Alexa Fluor 488 azide	Thermo Fisher Scientific	A10266
DAPI (RRS)	DOJINDO	D523
DAPI (Immunofluorescence)	Thermo Fisher Scientific	D1306
Blasticidin S HCl (blasticidin)	Thermo Fisher Scientific	A1113902
Crystal Violet	Nacalai	09803-62
α-amanitin	Sigma	A2263
N,N'-Disuccinimidyl Glutarate (DSG)	Wako	041-32823
Bovine Serum Albumin heat shock fraction (BSA)	Sigma	A7906
UltraPure Water	Wako	214-01301
proteinase K	Wako	169-21041
high-fidelity KAPA HiFi PCR Enzyme	Roche	KK2102
Tissue-Tek O.C.T. Compound	Sakura finetek	4583
normal goat serum	Cedarlane	CL1200
normal donkey serum	Jackson Immuno Research Laboratories	017-000-121
Osmium tetroxide	Nacalai	25728-04
Toluidine Blue O	WALDECK	1B481
Fluoromount/Plus	Diagnostic BioSystems	K048
Fisher Chemical Permount Mounting Medium	Thermo Fisher Scientific	SP15-100
Critical Commercial Assays		
GeneArt Precision gRNA Synthesis Kit (target sequence is described in the text)	Thermo Fisher Scientific	A29377
Protein Assay kit (Bradford)	Bio-Rad	500-0006
PTMScan Ubiquitin Remnant Motif (K-ε-GG) Kit	Cell Signaling Technologies	5562
Western Lightning Plus-ECL	PerkinElmer	NEL105001
ViraPower Packaging Mix	Thermo Fisher Scientific	K4975-00
PEG-it Virus Precipitation Solution	System Biosciences	LV810A-1
Strep-Tactin Sepharose 50% suspension	IBA Lifesciences	2-1201-002
GFP-Trap A Kit	Chromotek	gta-10
UbiCREST Deubiquitinase Enzyme Set	Boston Biochem	K-400
Protein A Agarose/Salmon Sperm DNA	Millipore	16-157
SureBeads Protein A/G Magnetic Beads	Bio-Rad	161-4833
MinElute PCR Purification Kit	QIAGEN	28006
NEBNext Ultra II DNA Library Prep Kit for Illumina	NEB	E7645S
NEBNext Multiplex Oligos for Illumina (Index Primers Set 1)	NEB	E7335S
preCR enzyme mix	NEB	M0309S
JB-4 Embedding Kit	Polysciences	00226-1
Deposited Data		
RPB1 ChIP-seq	This study	SRA, PRJNA548234, Run IDs in Table S7
Experimental Models: Cell Lines		
Human: HCT116 (colon cancer cell line)	RIKEN BRC	HCT116
Human: HCT116 Δ*UVSSA*	This study	N/A

(*Continued on next page*)

Continued

REAGENT or RESOURCE	SOURCE	IDENTIFIER
Human: HeLa (cervical cancer cell line)	laboratory stock	N/A
Human: HeLa RPB1-K163R	This study	N/A
Human: HeLa RPB1-K177R	This study	N/A
Human: HeLa RPB1-K642R/K643R	This study	N/A
Human: HeLa RPB1-K710R	This study	N/A
Human: HeLa RPB1-K767R	This study	N/A
Human: HeLa RPB1-K796R	This study	N/A
Human: HeLa RPB1-K812R	This study	N/A
Human: HeLa RPB1-K853R	This study	N/A
Human: HeLa RPB1-K866R	This study	N/A
Human: HeLa RPB1-K874R	This study	N/A
Human: HeLa RPB1-K1225R	This study	N/A
Human: HeLa RPB1-K1268R #7	This study	N/A
Human: HeLa RPB1-K1268R #9	This study	N/A
Human: HeLa RPB1-K1350R	This study	N/A
Human: HeLa Δ*CSB*	This study	N/A
Human: HeLa Δ*UVSSA*	This study	N/A
Human: HeLa *UVSSA*-ΔK414	This study	N/A
Human: HEK293 (SV40 transformed embryonic kidney cell line, 293FT)	Thermo Fisher Scientific	R70007
Human: HEK293 RPB1-K1268R	This study	N/A
Human: HEK293 Δ*CSA*	This study	N/A
Human: 48BR (dermal fibroblast, normal)	Nakazawa et al., (2010)	N/A
Human: CS10LO (dermal fibroblast, Cockayne syndrome, CS-B)	Nakazawa et al., (2010)	N/A
Human: XP15BR (dermal fibroblast, xeroderma pigmentosum, XP-A)	Nakazawa et al., (2010)	N/A
Human: XP21BR (dermal fibroblast, xeroderma pigmentosum, XP-C)	Nakazawa et al., (2010)	N/A
Experimental Models: Organisms/Strains		
Mouse: C57BL/6JJcl (wild type, BL/6)	CLEA Japan	N/A
Mouse: *Xpa*$^{-/-}$ (BL/6 background)	Nakane et al., (1995)	N/A
Mouse: *Polr2a*-K1268R (BL/6 background)	This study	N/A
Mouse: *Polr2a*$^{WT/WT}$ (WT/WT)	This study	N/A
Mouse: *Polr2a*$^{WT/K1268R}$ (WT/KR)	This study	N/A
Mouse: *Polr2a*$^{K1268R/K1268R}$ (KR/KR)	This study	N/A
Mouse: *Polr2a*$^{WT/WT}$ / *Xpa*$^{+/-}$	This study	N/A
Mouse: *Polr2a*$^{WT/K1268R}$ / *Xpa*$^{+/-}$	This study	N/A
Mouse: *Polr2a*$^{K1268R/K1268R}$ / *Xpa*$^{+/-}$	This study	N/A
Mouse: *Polr2a*$^{WT/WT}$ / *Xpa*$^{-/-}$	This study	N/A
Mouse: *Polr2a*$^{WT/K1268R}$ / *Xpa*$^{-/-}$	This study	N/A
Mouse: *Polr2a*$^{K1268R/K1268R}$ / *Xpa*$^{-/-}$ (DM)	This study	N/A
S. pombe: *h*$^{+}$ *ade6*-704 *leu1*-32 *ura4*-D18 *rpb1::loxP-rpb1*$^{+}$*-loxM* (NER^{+}/WT)	This study	N/A
S. pombe: *h*$^{+}$ *ade6-704 leu1-32 ura4-D18 rpb1::loxP-rpb1-K1252R-loxM* (NER^{+}/KR)	This study	N/A
S. pombe: *h*$^{+}$ *ade6-704 leu1-32 ura4-D18 rhp14::NatMX rpb1::loxP-rpb1*$^{+}$*-LoxM* (*rhp14*/WT)	This study	N/A

(*Continued on next page*)

Continued

REAGENT or RESOURCE	SOURCE	IDENTIFIER
S. pombe: *h*$^{+}$ *ade6-704 leu1-32 ura4-D18 rhp14::NatMX rpb1::loxP-rpb1-K1252R-LoxM* (*rhp14*/KR)	This study	N/A
S. pombe: *h*$^{+}$ *ade6-704 leu1-32 ura4-D18 rhp26::NatMX rpb1::loxP-rpb1*$^{+}$*-LoxM* (*rhp26*/WT)	This study	N/A
S. pombe: *h*$^{+}$ *ade6-704 leu1-32 ura4-D18 rhp26::NatMX rpb1::loxP-rpb1-K1252R-LoxM* (*rhp26*/KR)	This study	N/A
Oligonucleotides		
All oligonucleotide sequences used in this study are listed in the text and in Table S3	This study	N/A
Recombinant DNA		
pLenti-6.3-Myc-Strep-Ubiquitin (plasmid)	This study	N/A
pLenti-6.3-Myc-Strep-Ubiquitin-K-null (plasmid)	This study	N/A
pLenti-6.3-Myc-Strep-Ubiquitin-K6R (plasmid)	This study	N/A
pLenti-6.3-Myc-Strep-Ubiquitin-K11R (plasmid)	This study	N/A
pLenti-6.3-Myc-Strep-Ubiquitin-K29R (plasmid)	This study	N/A
pLenti-6.3-Myc-Strep-Ubiquitin-K33R (plasmid)	This study	N/A
pLenti-6.3-Myc-Strep-Ubiquitin-K48R (plasmid)	This study	N/A
pLenti-6.3-Myc-Strep-Ubiquitin-K63R (plasmid)	This study	N/A
pSpCas9(BB)-2A-Puro (px459)	Ran et al., (2013)	Addgene, 48139
pCMV-GFP-POLR2A (GFP-tagged α-amanitin resistant human RPB1)	Sugaya et al., (2000)	N/A
pCMV-GFP-POLR2A-K1268R (GFP-RPB1-K1268R)	This study	N/A
Software and Algorithms		
CRISPRdirect	Naito et al., (2015)	https://crispr.dbcls.jp
CRISPOR	Haeussler et al., (2016)	http://crispor.tefor.net
PTMscan	Cell Signaling Technologies	https://www.cellsignal.jp/contents/_/simplifying-proteomics/proteomics
SEQUEST tool in Proteome Discoverer 2.1	Thermo Fisher Scientific	https://www.thermofisher.com/store/products/OPTON-30945
Swiss-Prot	SIB, Swiss Institute of Bioinformatics	https://www.uniprot.org/
HCS Studio 2.0 in *ArrayScan* VTI system	Thermo Fisher Scientific	https://www.thermofisher.com/jp/ja/home/life-science/cell-analysis/cellular-imaging/high-content-screening/high-content-screening-instruments/hcs-studio-2.html
Trimmomatic (v3.36)	Bolger et al., 2014	http://www.usadellab.org/cms/?page=trimmomatic
Burrows-Wheeler Aligner (BWA-v0.7.12-r1039)	Li, (2013)	http://bio-bwa.sourceforge.net
Biobambam2 (v2.0.72)	Tischler and Leonard, (2014)	https://github.com/gt1/biobambam2
Genome Analysis Toolkit (GATK-v3.5)	McKenna et al., (2010)	https://gatk.broadinstitute.org

(*Continued on next page*)

Continued

REAGENT or RESOURCE	SOURCE	IDENTIFIER
Integrated Genome Viewer (IGV-v2.3.90)	Thorvaldsdóttir et al., (2013)	https://software.broadinstitute.org/software/igv/
R (v3.5.1)	The R Development Core Team	https://www.r-project.org
ngs.plot.r (v2.63)	Shen et al., (2014)	https://github.com/shenlab-sinai/ngsplot
samtools (v. 1.9)	Li et al., (2009)	http://www.htslib.org/doc/
Bedtool (v2.27.1)	Quinlan and Hall, (2010)	https://bedtools.readthedocs.io/en/latest/#
deepTools (v3.1)	Ramírez et al., (2014)	https://deeptools.readthedocs.io/en/3.0.1/content/tools/computeMatrix.html
edgeR (v3.24.3)	Robinson et al., (2010)	https://bioconductor.org/packages/release/bioc/html/edgeR.html
KEGG (Kyoto Encyclopedia of Genes and Genomes) pathway	Kanehisa and Goto, (2000)	https://www.genome.jp/kegg/kegg_ja.html
g:Profiler (version e95_eg42_p13_f6e58b9)	Raudvere et al., (2019)	https://biit.cs.ut.ee/gprofiler/gost
3D Slicer (4.10.2)	Fedorov et al., 2012	https://www.slicer.org/
Other		
electroporator	NepaGene	NEPA21
NEPA21 electroporator electrode for electroporation	NepaGene	CUY505P5
ultraviolet (UV) crosslinker	Funakoshi	CL-1000
digital radiometer (UV)	Funakoshi	UVP/97-0015-02
homogenizer	TOMY	UD-211
homogenizer tip	TOMY	TP-040
Sep-Pak C18 Classic column	Waters	WAT051910
Pierce C18 Tips (stage)	Thermo Fisher Scientific	87782
C18 packed emitter column (3 μm particle, 75 μm × 15 cm)	Nikkyo Technos	N/A
Ultimate 3000, HPLC system	Thermo Fisher Scientific	N/A
Orbitrap QE, High-resolution accurate-mass system	Thermo Fisher Scientific	N/A
SuperSep Ace, 6%, 13well	Wako	195-15171
SuperSep Ace, 5-20%, 17well	Wako	194-15021
FluoroTrans PVDF Transfer Membrane	PALL	BSP0161
ImageQuant LAS 4000mini	GE Healthcare	N/A
Falcon 96 Well Cell Culture Plate, Clear, Flat Bottom, Tissue Culture Treated	Corning	353072
ArrayScan VTI system (high contents imaging)	Thermo Fisher Scientific	N/A
Illumina Hiseq NGS sequencer	Illumina	N/A
Ultrasonicator	Covaris	M220
CosmoScan FX system	RIGAKU	N/A
NEO Micro Cover Glass, 24 × 60 mm	Matsunami Glass	C024601
confocal laser microscope LSM700 system	Carl-Zeiss	N/A
microtome	Leica	RM2245
microscope Eclipse 55i system	Nikon	N/A

LEAD CONTACT AND MATERIALS AVAILABILITY

Further information and requests for resources and reagents should be addressed to the Lead Contact, Tomoo Ogi (togi@riem.nagoya-u.ac.jp), Department of Genetics, Research Institute of Environmental Medicine (RIeM), Nagoya University, Nagoya, Japan. All unique / stable reagents generated in this study are available from the Lead Contact with a completed Materials Transfer Agreement.

EXPERIMENTAL MODEL AND SUBJECT DETAILS

Human cell lines and culture

The following cell lines were used in this study: HCT116, human colon cancer cell line (RIKEN BRC, HCT116); HeLa, human cervical cancer cell line; HEK293, SV40-immortalized normal human embryonic kidney cells (Thermo Fisher Scientific, R70007); 48BR, normal human primary fibroblast (Nakazawa et al., 2012); CS10LO, primary fibroblast from CS-B individual (Nakazawa et al., 2012); XP15BR, primary fibroblast from XP-A individual (Nakazawa et al., 2012); XP21BR primary fibroblasts from XP-C individual (Nakazawa et al., 2012). Gene edited cells were listed in Table S3. All cells were maintained in DMEM (Wako, 043-30085) supplemented with 10% fetal bovine serum (FBS, Thermo Fisher Scientific, 10437-028) and antibiotics (Penicillin-Streptomycin, Wako, 168-23191), unless otherwise noted.

Mice

Xpa$^{-/-}$ mice are kind courtesy of Dr. Kiyoji Tanaka (Nakane et al., 1995). C57BL/6JJcl mice were purchased from CLEA Japan. All mice analyzed in this study were C57BL/6 background and were age/sex matched unless otherwise noted (age/sex of mice were described in the main text, figure legends, and in Tables S4–S6). *Polr2a*-K1268R knock-in mice were generated using CRISPR-Cas9 technology with the following reagents: recombinant Cas9, Alt-R S.p. Cas9 Nuclease 3NLS (Integrated DNA Technologies, IDT, 1074181); guide RNA (gRNA), GeneArt Precision gRNA Synthesis Kit (target sequence, 5′-TGATGAAAACAA GATGCAAG-3′) (Thermo Fisher Scientific, A29377); ssODN: IDT 4nmol Ultramer DNA Oligo (ssODN, 5′-ATGCAGAGA AGCTGGTCCTTCGAATCCGCATCATGAACAGTGATGAAAACA [**G***] GATGCA [g**] GAGGTAAATGGTCTGAGACCCGGGGGAAATA AAATAGAATGGGA-3′) (IDT). To design gRNA sequence, CRISPRdirect (Naito et al., 2015) and CRISPOR (Haeussler et al., 2016) are used for predicting unique target sites throughout the mouse genome. *Polr2a-K1268R target mutation; **silent mutation. Pronuclear-stage mouse embryos were prepared by thawing frozen embryos (CLEA Japan), and cultured in a KSOM medium (ARK Resource, KSOM). For EL, 100-150 embryos at 1 h after thawing were placed into a chamber with 40 μL of serum free media (Opti-MEM I, Thermo Fisher Scientific, 31985062) containing 100 ng/μl Cas9 protein, 200 ng/μl gRNA, and 300 ng/μl ssODN. They were electroporated with a 5mm gap electrode (NepaGene, CUY505P5) in a NEPA21 Super Electroporator (Nepa Gene). The poring pulses for the electroporation were voltage 225 V, pulse width 1ms for mouse embryos, pulse interval 50 ms, and number of pulses 4. The first and second transfer pulses were voltage 20 V, pulse width 50 ms, pulse interval 50 ms, and number of pulses 5. Mouse embryos that developed to the two-cell stage after the electroporation were transferred into the oviducts of female surrogates anesthetised with sevoflurane (Mylan, 1900AMX00269). The animals were kept under conditions of 50% humidity and a 12 h:12 h light:dark cycle. They were fed a standard pellet diet (Oriental Yeast, MF) and tap water *ad libitum*, unless otherwise noted. Mice strains described in this study were obtained from the crossbred littermates. DM mice were supplied with gelled water and softened food pellets, to exclude the possibility that the inability to feed causes these phenotypes. All the animal studies were conducted in compliance with the ARRIVE guidelines. The experiments using genetically modified mice were approved by the Animal Care and Use Committee and the recombinant DNA experiment committee of Nagoya University and Osaka University.

S. pombe

Standard *S. pombe* genetics and molecular biology techniques were employed as described previously (Moreno et al., 1991). *rpb1*-K1252R cells were constructed by replacing the endogenous *rpb1* on *S. pombe* (501) genome with the sequence of the mutated *rpb1* gene based on the Cre-loxP method (Watson et al., 2008). The *rhp14* and *rhp26* deleted strains were created by PCR based integration of NatMX gene as described previously (Bähler et al., 1998). The integration of NatMX at *rhp14* and *rhp26* loci was verified by PCR as well as their UV sensitivity.

METHOD DETAILS

Gene editing by CRISPR/Cas9

To achieve NER gene knock-outs and the endogenous *POLR2A* gene deletion, as well as to generate RPB1-KR mutant cells, we employed CRISPR/Cas9-based gene editing strategy (Ran et al., 2013). For a gene deletion experiment, a guide RNA (gRNA) coding sequence was cloned into px459 vector (Addgene, 48139). The plasmid (3 μg DNA per 1 × 10^7 cells) was transfected into designated cells using Lipofectamine 2000 (Thermo Fisher Scientific, 11668019). 24 h after transfection, cells were selected for 48 h with 40 μg/ml puromycin (Nacalai, 29455-54) in DMEM (10% FBS). Single clones were isolated from surviving fraction by limiting dilution. Knock-outs were confirmed by direct Sanger sequencing of PCR-amplified genomic DNA and by the lack of designated protein expression by immunoblotting.

Generation of RPB1-KR mutants were achieved by inducing site-specific double-strand breaks near the designated RPB1 lysine residues in combination with homology-directed-repair (HDR) oligonucleotides carrying the KR substitutions. A ~100 bp designated HDR oligonucleotide was co-transfected with a gRNA expressing plasmid corresponding to the target sequence. The introduction of designated amino acid substitution and the lack of wild-type RPB1 expression were confirmed by Sanger sequencing of genomic DNA, and RNA sequencing as appropriate.

All gRNA and HDR sequence information are listed in Table S3. Experiments using RPB1-K1268R HeLa cells, clone #9 was used throughout the study unless otherwise noted.

SILAC mass-spectrometry

Wild-type and Δ*UVSSA* HCT116 cells were grown for at least 6 doublings in DMEM for SILAC (Thermo Fisher Scientific, 11668019), lacking conventional arginine and lysine, supplemented with 10% dialysed FBS (SAFC Biosciences, 12117C), as well as unlabeled L-arginine and L-lysine (Light-wild-type, Thermo Fisher Scientific, 89989 and 89987), or stable-isotope labeled L-arginine (^{13}C6-^{15}N4) and L-lysine (^{13}C6-^{15}N2) (Heavy-Δ*UVSSA*, Wako, 010-24041 and 123-06081). 1h after10 J/m^2 UV irradiation using a UV crosslinker (CL1000, Funakoshi) and a UV-fluence meter (UVP-97, Funakoshi), cells were lysed in Urea Lysis buffer (20 mM HEPES pH 8.0, 1 mM beta-glycerophosphate, 8 M urea, 2.5 mM sodium pyrophosphate, and 1 mM Na3VO4) with sonication (15 s, power 0.25%; TOMY, UD-211 homogenizer equipped with TP-040 tip). Protein quantitation was performed using Bradford Protein Assay kit (Bio-Rad, 500-0006), and Light- and Heavy-labeled proteins were combined in 1:1 ratio.

Protein samples were reduced with 5 mM 1,4-dithiothreitol (Thermo Fisher Scientific, R0861) for 30 min at 50°C, and subsequently alkylated with 10 mM iodoacetamide (Millipore, 144-48-9) for 15 min. The protein samples were then digested for 4 h with Lysyl Endopeptidase (Lys-C, Wako, 125-05061) at 1:100 enzyme: substrate ratio, followed by additional overnight digestion with trypsin (Thermo Fisher Scientific, 90059) at 1:50 enzyme: substrate ratio at 37°C. Digested peptides were purified using Sep-Pak C18 columns (Waters, WAT051910). Eluted peptides were completely dried by lyophilisation. For the enrichment of diGly peptides, anti-ubiquitin remnant motif (K-ε-GG) antibodies conjugated to beads were used (PTMscan kit, Cell Signaling Technologies, 5562). The peptides were dissolved in IAP buffer (50 mM MOPS, 10 mM sodium phosphate and 50 mM NaCl, pH 7.2), and the supernatant was incubated with one-half of the beads for 2 h at 4°C on a rotator unit. After centrifugation, the supernatant was incubated again with the remaining bead for 2 h at 4°C. The beads were then washed twice with ice cold IAP buffer, and subsequently 3 times with ice cold HPLC-grade water. The peptides were eluted using 2 cycles of 0.15% TFA. Finally, the eluted peptides were desalted using C18 stage tips (Thermo Fisher Scientific, 87782) and completely dried using vacuum centrifugation.

Peptide fractions were analyzed on Ultimate 3000 (Thermo Fisher Scientific) nano-HPLC, connected to Orbitrap Q-Exactive mass-analyzer system (Thermo Fisher Scientific) equipped with a nanoelectrospray source. Peptides were separated on a 15cm analytical column (75 μm inner diameter) with 3 μm C18-beads (Nikkyo Technos). Each peptide fraction was separated using a 135 min gradient ranging from 2% to 35% acetonitrile in 0.1% formic acid at a flow rate of 300 nL/min. The washout followed at 95% acetonitrile in 0.1% formic acid for 20 min. Spray voltage was set to 1.8 kV, s-lens RF level at 50, and heated capillary temperature 250°C. All experiments were performed in the data-dependent acquisition mode to automatically isolate and fragment top10 multiply-charged precursors (+2, +3, +4 and +5) according to their intensities. Former target ions were dynamically for 15 s excluded and all experiments were acquired using positive polarity mode. Full scan resolution was set to 70,000 at m/z 200 and the mass range was set to m/z 350-1800. Full scan ion target value was 1×10^6 allowing a maximum fill time of 60ms. Higher-energy collisional dissociation (HCD) fragment scans was acquired with optimal setting for parallel acquisition using 2.0 m/z isolation width and normalized collision energy of 28.

Detection of RPB1 ubiquitination site in UV irradiated HeLa cells

Mass-spectrometry was performed for UV irradiated HeLa cells cultured in standard DMEM. The wild-type HeLa cells were UV irradiated (20 J/m^2), followed by incubation for 1 h. Sample preparation and the enrichment of ubiquitin remnant peptides were as described above.

Mass-spec raw data processing and analysis

The data were analyzed using SEQUEST tool in Proteome Discoverer 2.1 (Thermo Fisher Scientific) and searched in the complete human proteome database (Swiss-Prot, SIB). The mass tolerances for the precursor and fragment were 10 ppm and 0.02 Da, respectively. Cysteine carbamidomethylation was included as a fixed modification, and N-terminal protein acetylation, methionine oxidation and lysine ubiquitlation were included as variable modifications. Peptide identification was filtered at a false discovery rate (FDR) < 1%.

Detection of ubiquitinated RPB1-IIo by immunoblotting

Details are described previously (Nakazawa et al., 2012). Cells were UV irradiated (20 J/m^2 254 nm UVC), followed by 1 h incubation unless otherwise noted. Whole cell lysate (for primary cells) was prepared by dissolving cells in SDS lysis buffer (0.2 M Tris HCl pH6.8, 10% Glycerol, 2.5% SDS, 0.1 M DTT). Chromatin fraction was prepared by extracting cells in isotonic extraction buffer, EB (50 mM Tris HCl pH 7.5, 150 mM NaCl, 2 mM $MgCl_2$) with 0.5% NP-40 (Wako, 198596) and 5 × cOmplete protease inhibitor (Roche, 5056489001), for 30 min at 4°C (nuclear/cytoplasm fraction), followed by further 1 h incubation of the pellets with 100 U/ml Benzonase (Millipore, 70664) in EB buffer (chromatin fraction). Protein samples were resolved by 6% (Wako, 195-15171) or 5%–20% (Wako, 194-15021) gradient SDS-PAGE gels. The elongating form of RNA polymerase II (RNA polIIo, RPB1-IIo) large subunit (RPB1) was detected by immunoblotting with anti phospho-Ser2-CTD antibody (3E10, Millipore, 04-1571) against the Ser2-phosphorylated (phospho-Ser2) carboxy-terminal domain (CTD) heptapeptide ($YS_2PTS_5PS_7$) repeat (RPB1-Ser2), which is a marker of RPB1-IIo. 10 μM MLN4924 (ChemScene, CS-0348) / 0.01% DMSO (Sigma, D5879) treatment were performed 1 h prior to UV irradiation.

Recovery of RNA Synthesis (RRS) assay and basal transcription measurement

Details are described previously (Nakazawa et al., 2010). Briefly, cells were cultured in DMEM (10% FBS) and plated in plastic 96well plates (Corning, 353072). Cells were UV irradiated (5-13 J/m^2 254 nm UVC unless otherwise noted), followed by 12 h incubation for RNA synthesis recovery. RRS levels and basal transcription were measured by the fluorescence-based ethynyluridine (EU)-incorporation assay (Jia et al., 2015; Limsirichaikul et al., 2009; Nakazawa et al., 2010). Concisely, recovered cells as well as non-irradiated cells were incubated for 2 h in media supplemented with 100 μM 5-ethynyluridine (5-EU, Thermo Fisher Scientific, E10345), followed by fluorescent-azide conjugation (Click-chemistry, Thermo Fisher Scientific): Cells were fixed and permeabilised for 20 min in PBS (Wako, 045-29795) containing 2% paraformaldehyde and 0.5% Triton X-100. After washing with PBS, cells were then incubated with coupling buffer with 10 μM Alexa Fluor 488 azide (Thermo Fisher Scientific, A10266), 50 mM Tris-HCl (pH 7.3), 4 mM $CuSO_4$, 10 mM sodium ascorbate, and 30 ng/ml DAPI (DOJINDO, D523) for 60 min, followed by washing with PBST (0.05% Tween 20). Nuclear fluorescent image acquisition and data processing were automated with HCS Studio 2.0 software in the *ArrayScan VTI* system (Thermo Fisher Scientific).

Lentivirus and complemented cells

The wild-type human *UVSSA* cDNA cloned into the pLenti6 viral vector was described previously (Nakazawa et al., 2012). The amino acid substitution mutants, K414R, F408A, and V411A, were generated from the wild-type *UVSSA* vector plasmid by site-directed PCR mutagenesis (this study and Okuda et al., 2017). For lentivirus production, HEK293 cells were transfected with the *UVSSA* plasmids together with ViraPower Packaging Mix (Thermo Fisher Scientific, K4975-00) using Lipofectamine 2000 (3 μg pLenti6-vector and 9 μg packaging plasmids mixture per 1 × 10^7 cells). Viral particles were collected 48 h after transfection and concentrated using PEG-it Virus Precipitation Solution (System Biosciences, LV810A-1). For virus complementation experiments, those lentiviruses were infected into Δ*UVSSA* HeLa cells and surviving fractions were expanded with 10 μg/ml blasticidin (Thermo Fisher Scientific, A1113902) prior to RRS assay and immunoprecipitation experiments.

UV clonogenic Survival assay

Details were described previously (Kashiyama et al., 2013). The wild-type and the RPB1-KR mutants, as well as Δ*CSB*, and Δ*UVSSA* HeLa cells were counted and plated into 6 well plastic dishes 24 h before UV irradiation. Cells were UV irradiated (1.25-5 J/m^2 254nm UVC) and incubated for 2 wk. Colonies were stained with crystal violet (Nacalai, 09803-62) and counted under a microscope (colonies with > 50 cells were scored as surviving fraction).

Ubiquitin pull-down assay

Plasmids harboring Strep-tagged wild-type or designated Ubiquitin-KR mutants (WT, wild-type; K null, no lysine residues; K6R, K11R, K27R, K29R,K33R, K48R, and K63R) were transfected using Lipofectamine 2000 and expressed in HeLa cells (wild-type, RPB1-K1268R, Δ*CSA*) or in the wild-type HEK293 cells 48 h prior UV irradiation. Cells were UV irradiated (20 J/m^2 254nm UVC), followed by 1 h incubation before whole cell lysate preparation. 1.5 × 10^7 cells were suspended in 1 mL SDS-denaturing buffer (20 mM Tris HCl pH 7.5, 50 mM NaCl, 0.5% Sodium Deoxycholate, 0.5% NP-40, 0.5% SDS, 1mM EDTA, 1 mM DTT, 1 × cOmplete protease inhibitor), followed by sonication (15 s, power 0.25%; UD-211, TP-040 tip). Affinity purification was performed by incubation of the lysate with 30 μL Strep-Tactin conjugated Sepharose beads (IBA Lifesciences, 2-1201-002) for 6 h at 4°C. After extensive washing with the SDS-denaturing buffer, the beads were resuspended in SDS lysis buffer with 0.025% bromphenol blue (BPB). Ubiquitinated RPB1 was detected with the anti-phospho-Ser2 CTD 3E10 antibody. Total ubiquitinated proteins were detected with an anti-myc-tag antibody (MBL, M192-7).

GFP pull-down assay

A plasmid vector expressing the GFP-tagged α-amanitin resistant human RPB1 (GFP-RPB1) was a kind courtesy of Dr. Sugaya (Sugaya et al., 2000). The RPB1-K1268R mutation was introduced into the wild-type vector plasmid by site-directed PCR mutagenesis. HEK293 cells expressing the GFP-RPB1 proteins (wild- type or K1268R mutant) were generated single clones were isolated prior to the experiments. Briefly, the GFP-RPB1 plasmids were transfected into HEK293 cells and selected with 10 μg/ml α-amanitin (Sigma, A2263). Endogenous RPB1 (all) and CSA (if indicated) were then sequentially knocked out respectively by the RPB1- and CSA- targeting CRISPR/Cas9 constructs as described above. Cells were UV irradiated (20 J/m^2 254nm UVC), followed by 1 h incubation before cell lysate preparation. SDS-denatured total cell lysates were prepared using the SDS-denaturing buffer (1.5 × 10^7 cells in 1 ml) as described above and affinity purification was performed by incubation of the lysate with 20 μL GFP-Trap agarose beads (Chromotek, gta-10) for 6 h at 4°C. After extensive washing with the SDS-denaturing buffer, the beads were resuspended in SDS lysis buffer with 0.025% BPB. Ubiquitinated and unmodified GFP-RPB1 were detected with the anti-RPB1-Ser2 3E10 antibody, and with an anti-GFP, B-2 antibody (Santa Cruz, sc-9996). Ubiquitinated proteins were detected with the following antibodies: P4D1 (Santa Cruz, sc-8017) detects total ubiquitinated proteins; Apu2 (Millipore, 05-1307) and HWA4C4 (eBioscience, 14-6077-80) respectively detect K48- and K63-linkage specific polyubiquitin chains.

Ubiquitin chain trimming by USP2

Ubiquitinated GFP-tagged RPB1 protein (wild-type) was partially purified from UV irradiated (1 h after 20 J/m^2) HEK293 cells. Briefly, 1.5 × 10^7 cells were suspended in 1 mL EBC buffer (50 mM Tris HCl pH 7.5, 150 mM NaCl, 0.5% NP-40, 1 mM EDTA, 1 × cOmplete protease inhibitor), followed by sonication (15 s, power 0.25%; UD-211, TP-040 tip). Affinity purification was performed by incubation of the lysate with 20 μL GFP-Trap agarose beads for 6 h at 4°C. After extensive washing with the EBC buffer without protease inhibitor, the beads were resuspended in 50 μL 1 × DUB reaction buffer with 1 × $USP2_{CD}$ ubiquitin protease enzyme (UbiCREST Deubiquitinase Enzyme Set, Boston Biochem, K-400) and incubated for 30 min at 37°C. Cleaved ubiquitin and GFP-RPB1 were detected as described above.

Co-immunoprecipitation

Details were described previously (Nakazawa et al., 2012). The wild-type and the RPB1-KR mutants, as well as Δ*CSA*, Δ*CSB*, and Δ*UVSSA* (also including UVSSA-ΔK414, and Δ*UVSSA* complemented with lentivirus expressing UVSSA mutants) HeLa cells were UV irradiated (20 J/m^2) and incubated for 1h unless otherwise noted. Crude native chromatin fractions were prepared as described above. Co-immunoprecipitation (IP) was performed for 2 h incubation on a rotator at 4°C with 1 mL chromatin lysate prepared from 2 × 10^7 cells and 2 μg of anti-RPB1-phospho Ser2-CTD antibody (Abcam, Ab5095) for RNAPIIo-Ser2 IP, Ser5-CTD 3E8 antibody (Millipore, 04-1572) for RNAPII-Ser5 IP, or anti-V5-tag antibody (MBL, PM003) for UVSSA-V5 IP. Immunocomplex were recovered by additional incubation with 20 μL protein A agarose beads (Millipore, 16-157) for 2 h on a rotator at 4°C. After extensive washing with high salt buffer (50 mM Tris HCl pH 7.5, 300 mM NaCl, 0.5% NP-40, 2 mM $MgCl_2$), the beads were resuspended in SDS lysis buffer with 0.025% BPB. Interactions were detected by immunoblotting with antibodies listed in the following sections. RPB1 in the complex was detected with the anti-phospho-Ser2 CTD 3E10, and the phospho-Ser5 CTD 3E8, antibodies.

Immunoblotting

Sample preparations are described in the above sections. Whole cell lysates or chromatin fraction, as well as affinity purified proteins or co-immunoprecipitated samples (IP) were resolved by 6% or 5%–20% gradient-SDS-PAGE gels (50 μg/lane, 13 well mini-gel). Unless otherwise noted, resolved protein samples were transferred to PVDF membranes (PALL, BSP0161), followed by blocking for 24 h at 4°C in 10% skim milk in TBST (50 mM Tris HCl pH 7.6, 150 mM NaCl, 0.05% Tween 20). The membranes were incubated with primary antibodies in 5% skim milk in TBST (0.05% Tween 20) for 24 h at 4°C. Primary antibodies are listed in the Key Resources Table (concentrations are described in the following section). Membranes were washed three times in TBST (0.05% Tween 20), followed by incubation with 1:1000 diluted HRP-conjugated secondary antibodies (Cell Signaling Technologies: anti-mouse, 7076; anti-rabbit, 7074; anti-rat, 7077) in 5% skim milk in TBST (0.05% Tween 20). After extensive washing with TBST (0.05% Tween 20), the proteins were detected using Western Lightning Plus-ECL (PerkinElmer, NEL105001), and images were captured by ImageQuant LAS 4000mini (GE Healthcare). SMC3, PCNA, and RAD21 are loading controls.

Primary antibody concentrations for immunoblotting

Rat monoclonal anti-RPB1-phospho-Ser2-CTD (RPB1-Ser2), 3E10, 1:1500 (Millipore, 04-1571); rat monoclonal anti-RPB1-phospho-Ser5-CTD (RPB1-Ser5), 3E8, 1:1000 (Millipore, 04-1572); mouse monoclonal anti-PCNA, PC-10, 1:1000 (NeoMarkers, MS-106-P0); rabbit polyclonal anti-Cul4A, 1:1000 (Bethyl Laboratories, A300-739A); mouse monoclonal anti-GFP, B-2, 1:1000 (Santa Cruz, sc-9996); mouse monoclonal anti- free-, mono-, and poly-ubiquitin, P4D1, 1:1000 (Santa Cruz, sc-8017); mouse monoclonal anti- mono-, and poly-ubiquitin, FK2, 1:1000 (ENZO Life Sciences, BML-PW8810); rabbit monoclonal anti-K48-linkage specific polyubiquitin, Apu2, 1:1000 (Millipore, 05-1307); mouse monoclonal anti-K63-linkage specific polyubiquitin, HWA4C4, 1:1000 (eBioscience, 14-6077-80); rabbit polyclonal anti-SMC3, 1:1000 (Bethyl laboratories, A300-060A); rabbit polyclonal anti-RAD21, D213, 1:2000 (CST, 4321); mouse monoclonal anti-TFIIH p89/XPB, G10, 1:1000 (Santa Cruz, sc-271500); mouse monoclonal anti-TFIIH p62/GTF2H1, G10, 1:500 (Santa Cruz, sc-48431); mouse monoclonal anti-CSB, 553C5a, 1:1000 (Bio Matrix Research, BMR00638); rabbit monoclonal anti-CSA, EPR9237, 1:1000 (Abcam, ab137033); mouse monoclonal anti-cdk7, MO1, 1:500 (MBL, K0068-3); mouse monoclonal anti-cdk9, D7, 1:200 (Santa Cruz, sc-13130); mouse monoclonal anti-Cyclin T1, E3, 1:100 (Santa Cruz, sc-271348); mouse monoclonal anti-SPT5, D3, 1:100 (Santa Cruz, sc-133217) mouse; polyclonal anti-UVSSA, 1:500 (Abnova, H00057654-B01P); HRP-conjugated mouse monoclonal anti-myc-tag, 1:1000 (MBL, M192-7).

Chromatin immunoprecipitation and NGS sequencing (ChIP-seq)

RPB1 chromatin immunoprecipitation (RPB1-ChIP) was performed under following conditions: The wild-type, RPB1-K1268R, Δ*CSA*, Δ*CSB*, and Δ*UVSSA* HeLa cells were UV irradiated (7 J/m^2 254nm UVC), followed by incubation for designated time periods for the time course experiments. Cells were cross-linked with 0.5 mg/ml N,N'-disuccinimidyl glutarate (DSG, Wako, 041-32823) in PBS for 1 h, followed by incubation with 1% formaldehyde in PBS for 20 min. Double-cross-linked samples (1 × 10^7 cells) were then suspended in 100 μL ChIP buffer (0.25% SDS, 1% Triton X-100, 150 mM NaCl, 1 mM EDTA, 0.5 mM EGTA, 20 mM HEPES pH 8.0), followed by sonication using Covaris M220 system (5% duty factor, 200 cycle, 960 s). After centrifugation at 14,000 rpm for 10 min, supernatants were pooled as chromatin-input samples (input). Immunoprecipitation of RPB1 was performed with anti-RPB1 phopho-Ser2-CTD (RPB1-Ser2: Ab5095, 3E10), or -Ser5-CTD (RPB1-Ser5: 3E8) antibodies, as well as with an anti-total RPB1 (pan-RPB1: A304-405A, Bethyl Laboratories) antibody in 500 μL ChIP buffer containing chromatin-input corresponding to 5 × 10^6 cells, 0.1% BSA

(Sigma, A7906), 1 × cOmplete protease inhibitor cocktail, and 3 μg designated anti-RPB1 antibodies. Samples were incubated for 18 h, followed by affinity purification with 20 μL IgG/A-conjugated magnetic beads (Bio-Rad, 161-4833). ChIP elutes (UltraPure Water, Wako, 214-01301) and chromatin-input samples were proceeded to de-cross-linking / protease treatment for 4 h at 65°C in a buffer containing 200 mM NaCl and 0.1 mg/ml proteinase K (Wako, 169-21041), followed by column purification (MinElute, QIAGEN, 28006).

Next-generation sequencing (NGS) libraries were prepared from 1 ng ChIPed DNA samples using NEBNext Ultra II DNA Library Prep Kit for Illumina (NEB, E7645S) and index primer sets (NEB, E7335S), unless otherwise noted. Strand-biased library amplification was performed using high-fidelity KAPA HiFi Enzyme (Roche, KK2102). The prepared libraries were sequenced under Illumina HiSeq 2500 system (Illumina), resulting in the production of 80bp single-end reads or 150 bp paired-end reads. Statistics of the sequence reads were summarized in Table S7.

Alignment of the ChIP-seq reads was performed as follows: Low-quality sequence reads and adapters were filtered out by Trimmomatic (v3.36) (Bolger et al., 2014). The trimmed reads were aligned to the human reference genome (GRC h37/hg19) with the Burrows-Wheeler Aligner (BWA-v0.7.12-r1039) (Li, 2013). Biobambam2 (v2.0.72) (Tischler and Leonard, 2014) was used to remove duplicate reads from the aligned reads. Sequence reads were locally realigned and base-quality scores were recalibrated with the IndelRealigner and BaseRecalibrator programs in Genome Analysis Toolkit (GATK-v3.5) (McKenna et al., 2010). The mapped reads were visualized with the Integrated Genome Viewer (IGV-v2.3.90) (Thorvaldsdóttir et al., 2013). Reproducibility was confirmed by calculating read counts per million mapped reads for individual genes, and their correlation was examined between replicates (Figure S4D).

The sequence data were deposited in the NCBI Short Read Archive (SRA), with BioProject accession number, PRJNA548234 (see also Table S7).

UV DNA damage removal from NGS library

For the preparation of DNA-repaired (damage-free) libraries, ChIPed DNA from UV-irradiated WT cells (3 h after 7 J/m^2) using Ab5095 antibody were treated with preCR enzyme mix (NEB, M0309S; a mixture of: T4 Endonuclease V, which cleaves cis-syn cyclobutane pyrimidine dimers; AP endonucleases; Taq DNA Ligase; Taq DNA polymerase) for 20 min or 2 h, before Illumina library adaptor ligation.

ChIP-seq meta gene profiles

From the aligned ChIP-seq reads, we generated meta-gene profiles to draw spatial distributions of RNAPIIo along gene bodies. Average numbers of reads per million mapped reads (RPM) within the gene bodies in 17,786 human protein-coding genes were counted with ngs.plot.r (v2.63) (Shen et al., 2014) using proportional bins. The values were normalized by the coverages of background mapped reads within 20 kb to 15 kb upstream regions from transcription start sites.

Calculation of the strand specificity index (SSI)

We defined the strand specificity index (SSI) as follows:

$$Strand\ specificity\ index(SSI) = \frac{fwd - rev}{fwd + rev}$$

where *fwd* and *rev* respectively denote the numbers of forwardly and reversely mapped reads in a gene body. This index deviates from zero when RPB1-ChIPed DNA fragments in Illumina NGS-libraries harbor abundant DNA lesions in the transcribed strands, because of the asymmetric adapters and a biased PCR amplification for the coding strands without DNA damage (Figures 4A and 4E). Positive and negative SSI values correspond to the bidirectional gene-orientation. To calculate SSI, 'first of pair strands' in ChIP-seq mapped reads were grouped according to their orientation (forward, reverse) using the samtools (v. 1.9) (Li et al., 2009). Subsequently, the numbers of forwardly and reversely mapped reads in the genic regions were counted using the BedIntersect program in Bedtool (v2.27.1) (Quinlan and Hall, 2010). The representative RefSeq transcripts, the same dataset calculated for the meta gene profile, were used to determine the SSI.

For further analyses, we selected 'actively transcribed genes', which displayed sufficient read counts of RPB1 ChIP adjacent to transcription start sites (TSS). In this study, we chose 9,836 'active' genes calculated from an pan-RPB1 ChIP-seq (see Figure S4C). Scatterplots of the SSI against read density in individual genes were created using the SmoothScatter in R. We also analyzed the temporal changes of the SSI across relative positions within gene bodies. The entire genic regions were divided into ten sub-regions of 10% bin; for each bin, the median of the SSI was calculated as its representative value.

Calculation of the Recovery Index (RI)

The temporal changes of the distributions of strand specificity across the active genes were monitored with the Recovery index (RI), a representative value of the SSI of individual genes. A distribution frequency of the gene-by-gene SSI may follow the Gaussian mixture model, comprising three normal distributions as represented by the following equation (see Figure S5A),

$$p(x) = \lambda N(x|\mu_0, \sigma_0) + \frac{1-\lambda}{2}\{N(x|\mu_1, \sigma_1) + N(x|-\mu_1, \sigma_1)\}$$

$$\mu_0 = 0, 0 \leq \lambda \leq 1$$

where the two peripheral normal distributions were presumed to be symmetric with respect to x = 0. From this equation, we define the Recovery index (RI) as follows.

$$Recovery\ index = \mu_1$$

This value denotes the distance of the peaks of the twin distributions from $x = 0$. The parameters of the Gaussian mixture model were estimated by employing maximum likelihood fitting with the fitdistr function in the MASS package of R.

Base resolution mapping of RNA polymerase IIo molecules at T-T dimer sites

We examined the enrichment of RNAPIIo molecules adjacent to T-T (A < > A in the coding strand) dimers (cyclobutane pyrimidine dimers, CPD; 6–4 pyrimidine–pyrimidone photoproducts, 6-4PP). ApA sites and franking 400 bp for both ends were extracted from the entire chromosome 1 of the hg19 genome sequence. Read coverages of each 5 bp bin were calculated with the computeMatix program in deepTools (v3.1) (Ramírez et al., 2014), and the results were visualized with the plotProfile in deepTools.

Gene-by-gene analysis for detecting unrepaired genes

We assumed a null hypothesis that the mapped read numbers in the coding and the template strands are not different. For every gene, the read number difference between the coding and the template strands were tested with edgeR v3.24.3 (Robinson et al., 2010) with read count normalization by the RLE method. The analyses were performed for all cell types using two to four replicates and *q*-values (Storey and Tibshirani, 2003) were calculated ($q < 0.05$ denotes statistically significant). Genes unrepaired in RPB1-K1268R cells but repaired in wild-type were subject to a gene enrichment analysis referring to the KEGG (Kyoto Encyclopedia of Genes and Genomes) pathway (Kanehisa and Goto, 2000). The analysis was performed using g:Profiler version e95_eg42_p13_f6e58b9 (Raudvere et al., 2019).

Computed tomography (CT)

CT images of animals were photographed (90 kV, 88 μA, FOV = 66 mm, whole body 8 s × 3 scans mode) using CosmoScan FX system (RIGAKU) under anesthesia with isoflurane (Pfizer,). Skeletal images were constructed using 3D Slicer software (4.10.2) (Fedorov et al., 2012).

Immunofluorescence of brain and spinal cord sections

Brains and lumbar spinal cords, dissected from mice transcardially perfused with 4% paraformaldehyde in phosphate buffer (4% PFA), were post-fixed with 4% PFA for 24 h, followed by cryoprotected in 30% sucrose in PBS for 48 h (brains) and 24 h (spinal cords). The samples were embedded in Tissue-Tek O.C.T. compound (Sakura finetek, 4583), followed by freezing at −80°C. Twelve μm cryosections were pre-incubated with in PBST (0.5% Triton X-100) for 30 min, followed by blocking with 5% normal goat serum (NGS, Cedarlane, CL1200) for brain sections, and 5% normal donkey serum (NDS, Jackson Immuno Research Laboratories, 017-000-121) for spinal cord sections, in PBST (0.3% Triton X-100) for 1 h.

The brain sections were immunostained for 24 h at 4°C with a primary antibody against GFAP (1:500, Sigma, G3893) in 5% NGS in PBST, followed by 2 h incubation with a fluorescent-dye-conjugated secondary antibody against mouse 1:1000 (Alexa Fluor 546, Thermo Fisher Scientific, A11030) IgG and 2.5 μg/mL DAPI (Thermo Fisher Scientific, D1306) in 5% NGS in PBST at RT. The spinal cord sections were immunostained for 1 h with primary antibodies against ChAT (1:100, Millipore, AB144P), Iba1 (1:500, Wako, 019-19741), and GFAP (1:500, Sigma, G3893), followed by 1 h incubation with fluorescent-dye-conjugated secondary antibodies against goat 1:1000 (Alexa Fluor 488, Thermo Fisher Scientific, A11055), rabbit 1:500 (Cy3, Jackson Immuno Research laboratories, 711-165-152), and mouse 1:500 (Alexa Fluor 647, Jackson Immuno Research laboratories, 715-605-150) IgGs and 2.5 μg/mL DAPI in 5% NDS in PBST at room temperature (RT). Coverslips (Matsunami Glass, C024601) were mounted with a drop of Fluoromount/Plus (Diagnostic BioSystems, K048) mounting medium. Images were captured using a confocal laser microscope (LSM700, Carl-Zeiss).

Semi-thin sections of 5th ventral roots

5th ventral roots, dissected from mice transcardially perfused with 4% paraformaldehyde in phosphate buffer (4% PFA), were post-fixed with 2% osmium tetroxide (Nacalai, 25728-04) in HEPES buffer for 2 h. Dehydration was performed with a graded series of alcohol as follows: 30%, 50%, 70%, and 80% ethanol for 10 min on ice each, and then 90%, 95%, and 99.5% (repeated twice) for 10 min at RT each. After dehydration, samples were embedded in JB-4 (Polysciences, 00226-1). One μm sections were prepared with a microtome (Leica, RM2245) and stained with 1% toluidine blue in 1% sodium borate for 30 s. Coverslips were mounted with a drop of Permount (Thermo Fisher Scientific, SP15-100) mounting medium. Images were captured using a microscope (Eclipse 55i, Nikon).

4NQO sensitivity assay

Exponentially growing *S. pombe* cells were sequentially diluted; 100 to 10-5 and spotted on plates of YEA containing indicated concentration of 4NQO (Sigma). These YEA plates were incubated for 3 days and scanned by ChemiDoc Touch MP system (Bio-Rad).

QUANTIFICATION AND STATISTICAL ANALYSIS

RRS and basal transcription measurement are based on quintuple wells and the graphs are presented as means (SD) unless otherwise noted. UV-survival data are based on triplicate of independent experiments and the plots are presented as means (SD). Mice body weights are presented as means (SD) of age / sex / genetic background matched animals unless otherwise indicated. Other details of statistical tests and quantifications used in this study are described in the corresponding parts of the main text, figure legends, or STAR Methods. All of the statistical tests were performed by using the packages or functions implemented in R (the edgeR package, and wilcox.test and fisher.test functions), except for the enrichment analysis with g:Profiler, which was performed on a web browser. A statistical significance was set at 0.05, and probabilities obtained from multiple comparisons were corrected.

DATA AND CODE AVAILABILITY

The ChIP-seq data were deposited in the NCBI Short Read Archive (SRA) under the BioProject ID, PRJNA548234. Individual Run IDs are listed in Table S7.

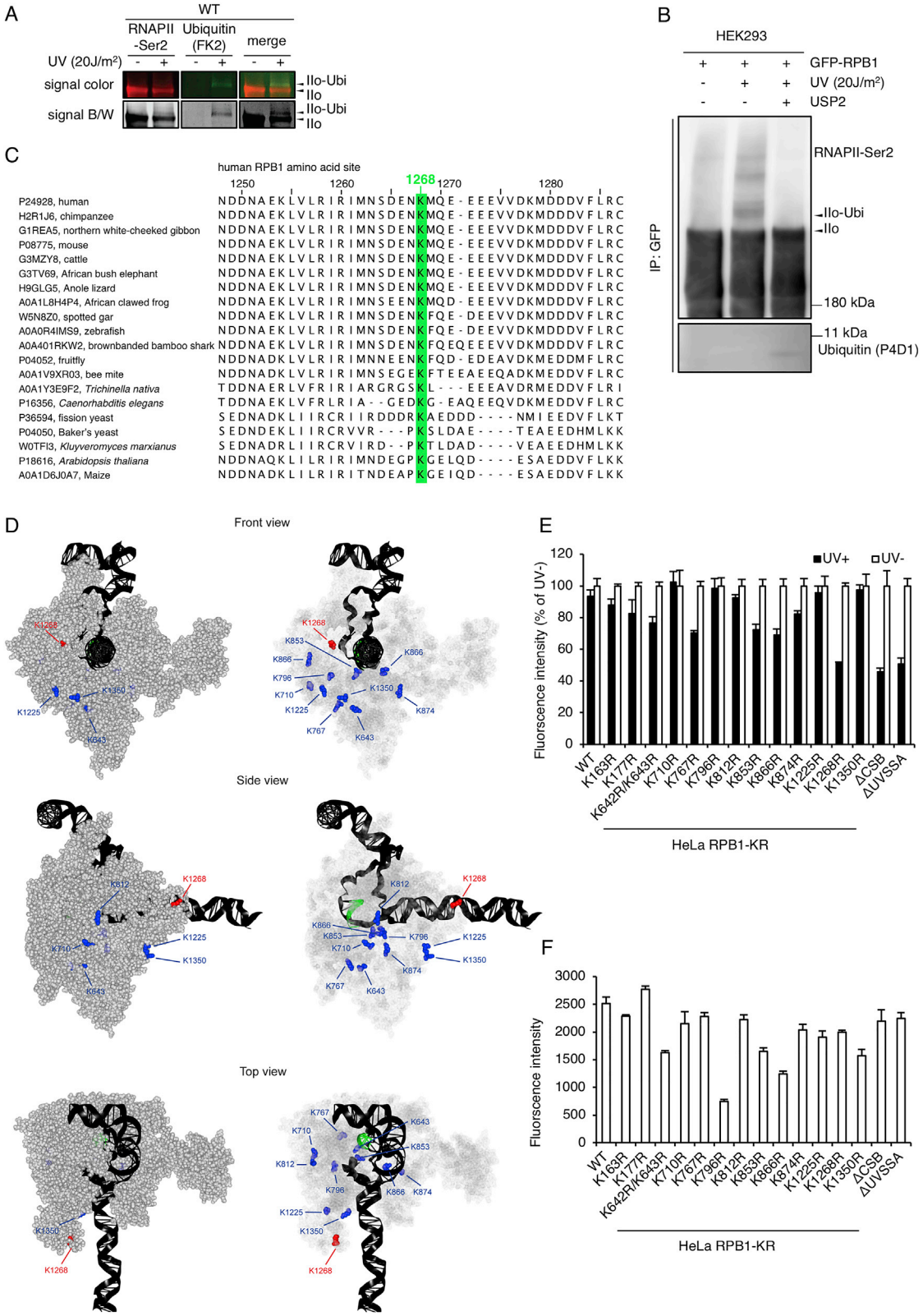

(legend on next page)

Figure S1. RNAPII Is Ubiquitinated at RPB1-K1268, Related to Figure 1

(A) Immunostainings of UV-induced RPB1-IIo upper bands overlap with staining for conjugated ubiquitin. The pictures are cropped from Figure 3D (WT, IP-RPB1-Ser2; RNAPII (Ser2), Ubiquitin; UV-, 1 h) and superimposed to indicate overlapping bands. Wild-type HeLa cells were UV irradiated (20 J/m^2), followed by 1h incubation. RPB1-IIo (red) and polyubiquitinated proteins (green) were respectively detected as described in Figure 3D.

(B) UV induced RPB1-IIo upper bands are consist of ubiquitin chains. Cells stably expressing GFP-tagged wild-type RPB1 (GFP-RPB1) were UV irradiated (20 J/m^2), followed by 1 h incubation. Affinity purification was performed with GFP-Trap conjugated beads under an SDS-denaturing condition. Partially purified GFP-RPB1 proteins were incubated with USP2 ubiquitin endoprotease. GFP-RPB1-IIo and cleaved ubiquitin were detected as described in Figure 2D.

(C) RPB1-K1268 is evolutionarily conserved in broad taxa. Multiple alignment was performed using MAFFT program. Amino acid residues correspond to human RPB1-K1268 is shown in green.

(D) RPB1-K1268 is surface-exposed near to where the downstream DNA enters RNAPII. RPB1 structures were reconstructed by CCP4MG software (v. 2.10.10) using the PDB data entry, 5IY9 (He et al., 2016). The K1268 residue is shown in red, while other putative ubiquitinated lysine residues are shown in blue.

(E) Recovery of RNA synthesis (RRS) after UV irradiation in RPB1-KR mutant HeLa cells shown in Figure 1B. WT, wild-type, Δ*CSB* and Δ*UVSSA* for controls. Cells were UV irradiated (closed bars, 5 J/m^2 UV; open bars, without UV), followed by 12h incubation for RNA synthesis recovery. RRS levels measured as in Figure 1C. Bars represent means (SD) of quadruple wells.

(F) Normal nascent transcription levels in RPB1-K1268R mutant. Ethynyluridine (EU)-incorporation for non-UV irradiated samples were shown. Fluorescent data obtained from Figure S1E. Bars represent means (SD) of quadruple wells.

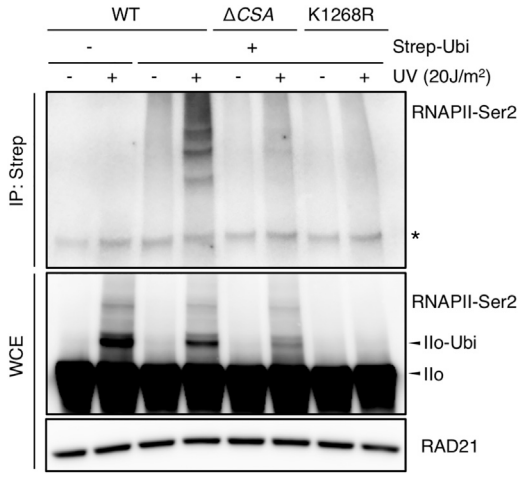

Figure S2. RPB1-K1268 Ubiquitination Is Dependent on CSA, Related to Figure 2

UV inducible ubiquitin chain formation on RPB1-K1268 residue. Strep-tagged Ubiquitin was transiently expressed in wild-type, Δ*CSA*, and RPB1-K1268R HeLa cells. Cells were 20 J/m^2 UV irradiated, followed by 1 h incubation. Affinity purification of ubiquitinated proteins was performed with Strep-Tactin conjugated beads under an SDS-denaturing condition. RPB1-Ser2 was detected as in Figure 1B. Discrete upper bands were detected in the UV irradiated wild-type cells and significant reduction of the bands was observed in the RPB1-K1268R and Δ*CSA* cells. RAD21, loading control (D213). Asterisk represents nonspecific products.

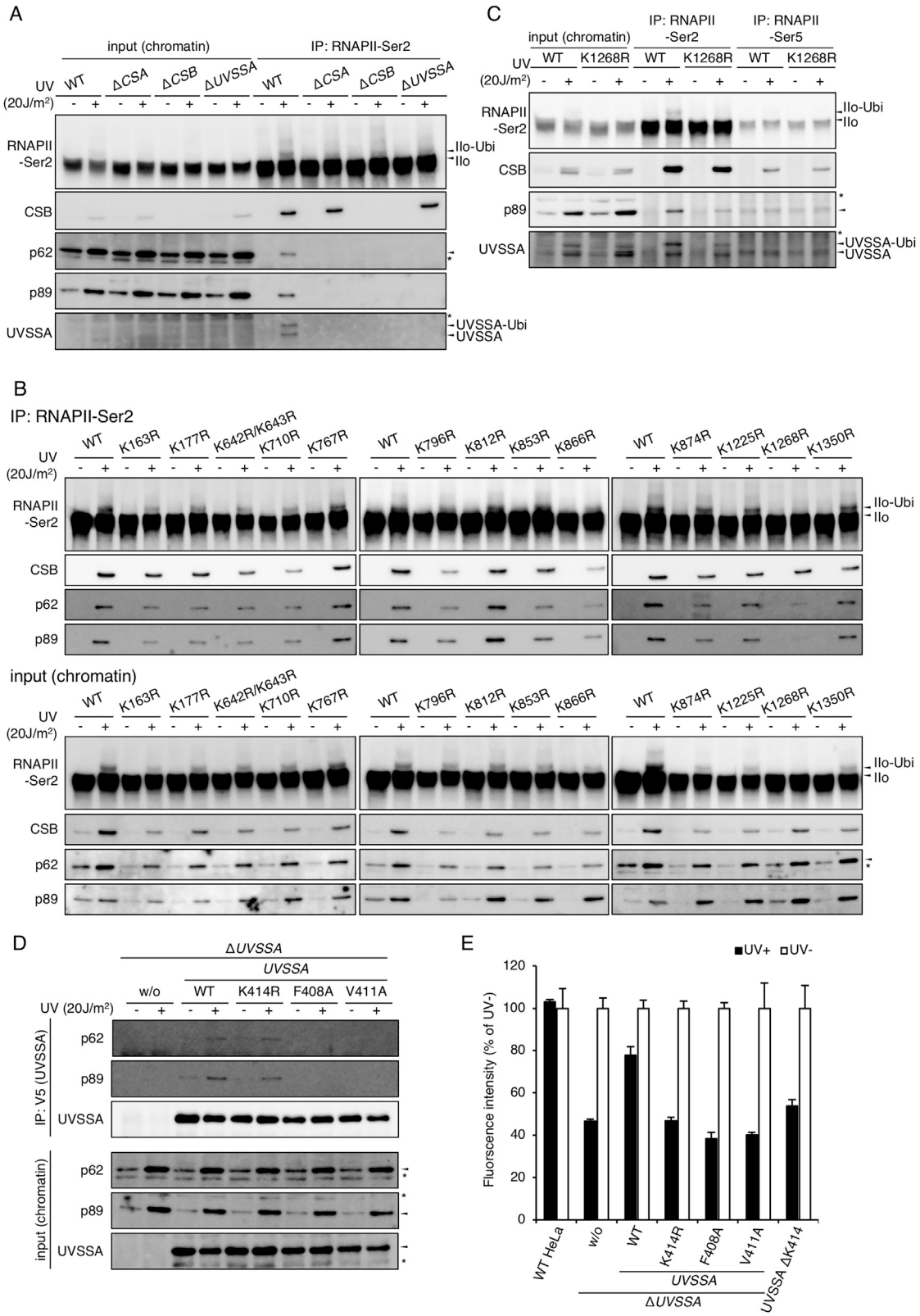

(legend on next page)

Figure S3. UVSSA Ubiquitination Regulates TFIIH Recruitment, Related to Figure 3

(A) CSA, CSB, and UVSSA are all required for the TFIIH recruitment to damage stalled RPB1 after UV irradiation. Wild-type (WT), Δ*CSA*, Δ*CSB*, and Δ*UVSSA* HeLa cells were UV irradiated (+, 20 J/m^2 UV, without UV), followed by 1h incubation. Co-immunoprecipitation of RPB1-Ser2 (Ab5095) and detection of interacting factors are as in Figure 3A.

(B) Normal TFIIH recruitment in RPB1-KR mutants except RPB1-K1268R. Wild-type (WT) and RPB1-KR mutant HeLa cells used in Figure 1B were UV irradiated (+, 20 J/m^2 UV, without UV), followed by 1h incubation. Co-immunoprecipitation of RPB1-Ser2 (Ab5095) and detection of interacting factors are as in Figure 3A.

(C) Normal TFIIH recruitment during transcription initiation in RPB1-K1268R mutant. Wild-type (WT) and RPB1-K1268R mutant HeLa cells were UV irradiated (+, 20 J/m^2 UV; -, without UV), followed by 1 h incubation. Co-immunoprecipitation of RPB1-Ser2 (Ab5095) and RPB1-Sre5 (3E8), as well as detection of interacting factors are as in Figure 3A. Recruitment of p89 was not abrogated in RPB1-K1268R mutant in RPB1-Ser5 immunoprecipitants.

(D) UVSSA-K414R mutant maintains TFIIH interaction. Δ*UVSSA* HeLa cells expressing the V5-tagged wild-type (WT) UVSSA and its PH-domain binding sequence (PDB) mutants (UVSSA-F408A, -V411A) as well as K414 mono-ubiquitination site mutant (UVSSA-K414R) were UV irradiated (+, 20 J/m^2 UV, without UV), followed by 1h incubation. Co-immunoprecipitation of V5-tagged UVSSA as well as detection of interacting factors are as in Figure 3A except using an anti-V5 antibody (PM003).

(E) UVSSA-PH-binding domain sequence (PDB) and mono-ubiquitination site are essential for TC-NER activity. HeLa cells used in Figures 3B and 3E were UV irradiated (6 J/m^2), followed by RRS measurements as described in Figure 1C. Bars represent means (SD) of triplicate wells.

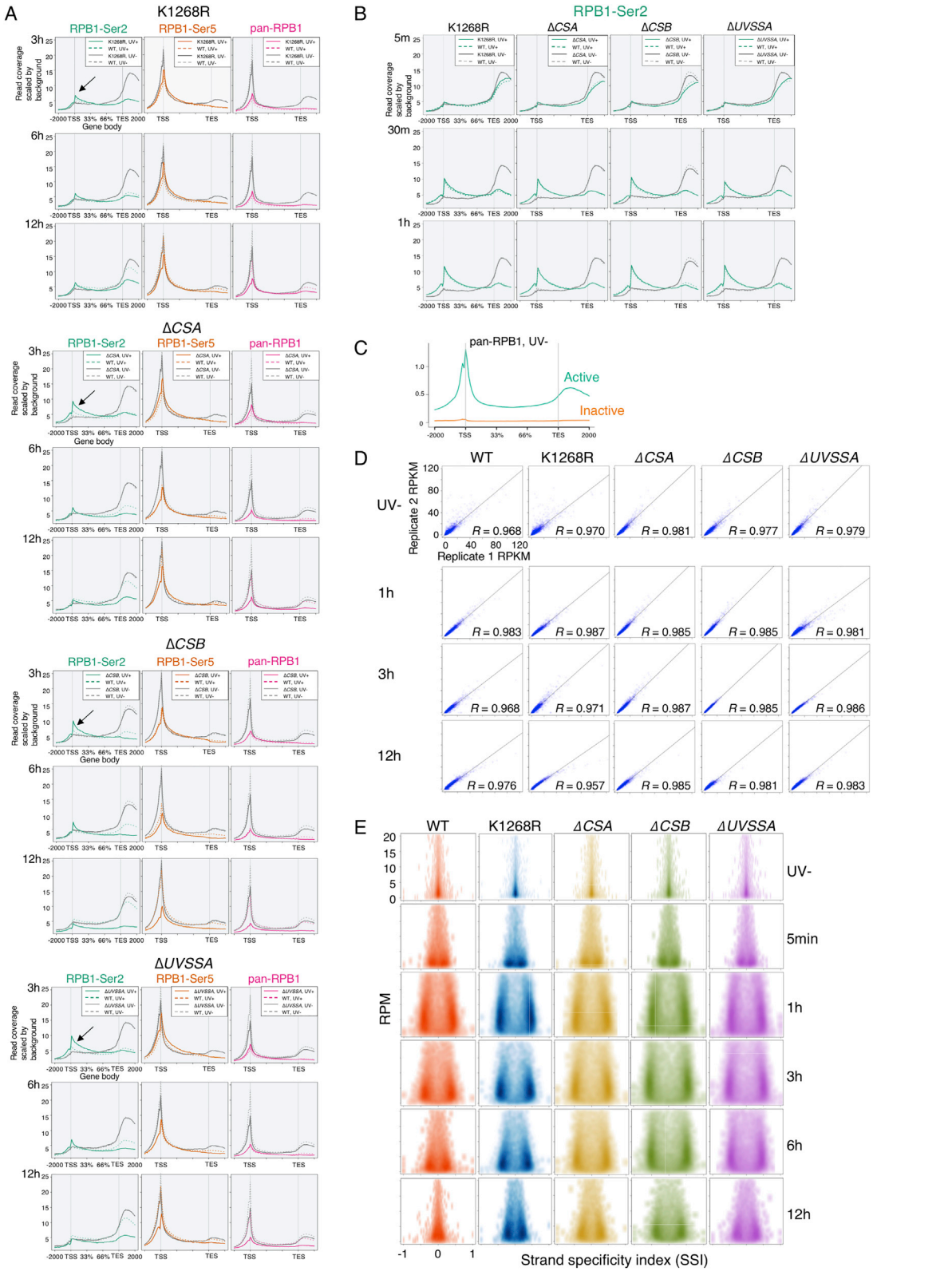

(legend on next page)

Figure S4. Strand-Specific ChIP-Seq for TC-NER Mutants, Related to Figure 4

(A) Distributions of chromatin-binding RNAPII molecules within gene bodies and flanking regions at designated time points after UV irradiation. ChIP-seq and analyses performed as in Figures 4B and 4C. ChIP-seq read coverage represents RNAPII distribution for wild-type (dashed lines, identical in the figures), RPB1-K1268R (K1268R), Δ*CSB*, Δ*CSA*, and Δ*UVSSA* (solid lines) HeLa cells (without UV, gray lines; 7 J/m^2 UV, colored lines for RPB1-Ser2, green; -Ser5, orange; and for total-RPB1 molecules, red). The Data for wild-type and RPB1-K1268R (without UV, 3 h, 12 h) are identical to which shown in Figures 4B and 4C. Arrows indicate the accumulation of RNAPII-Ser2 reads after UV near TSS in TC-NER-deficient cells.

(B) Distributions of chromatin-binding RPB1-Ser2 (3E10) within gene bodies and flanking regions at designated time points after UV irradiation (7 J/m^2). Early time points data for the cells in Figure S4A are shown. The Data for without UV are identical to which shown in Figure S4A.

(C) Determination of the 'active genes'. Pan-RPB1 ChIP-seq data from non-UV irradiated wild-type HeLa cells were used to determine the active genes as those exhibiting totally mapped reads nearby TSS (−100 to + 300 bp) > 0.6 reads per million mapped reads. Distributions of chromatin-binding RNAPII molecules (pan-RPB1) within gene bodies and flanking regions in active (green) and inactive (orange) genes are shown.

(D) Relationship of the mapped read depths of whole individual genes between biological replicates (RPB1-Ser2, 3E10, 7 J/m^2). Read depth was denoted by reads per kilobase of gene body per million mapped reads (RPKM). Spearman's correlation coefficient was calculated for each pair (n = 17,786).

(E) Scatterplots of SSI (RPB1-Ser2, 3E10, 7 J/m^2) against the density of mapped reads within individual 'active genes' (see Figure S4C) for wild-type (WT), RPB1-K1268R (K1268R), and TC-NER-deficient (Δ*UVSSA*, Δ*CSB*, Δ*CSA*) cells at designated time points. The plots of wild-type and RPB1-K1268R (without UV, 3 h, and 12 h) are identical to which shown in Figure 4G.

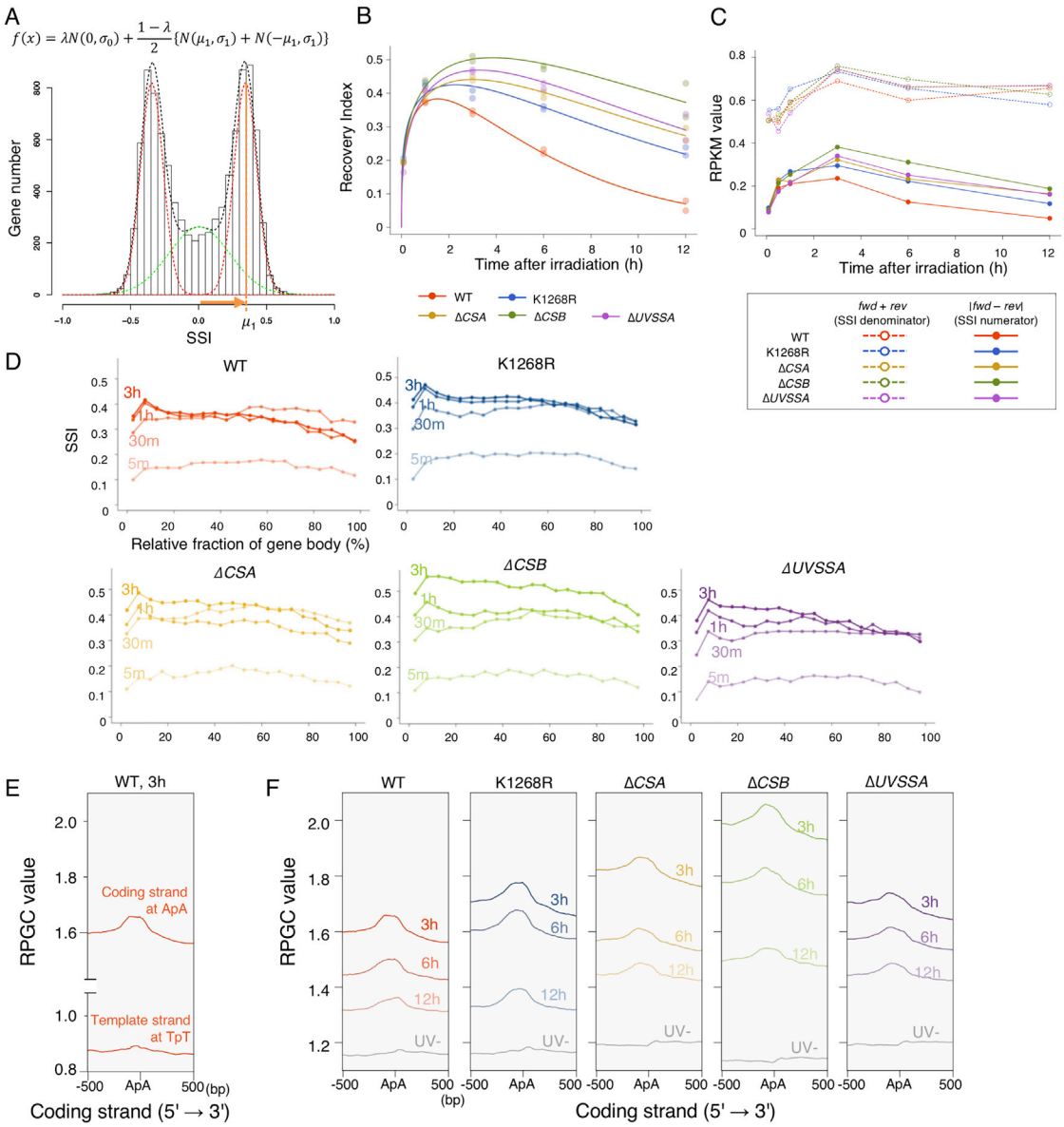

Figure S5. DNA Repair Kinetics of Transcribed Strands, Related to Figure 5

(A) Definition of Recovery index. We assume that a distribution frequency of the gene-by-gene strand specificity index (SSI) follows the mixed Gaussian distribution, comprising three normal distributions, where the two peripheral normal distributions are symmetric with respect to x = 0. The parameters were inferred with a maximum-likelihood framework using the fitdistr function implemented in the MASS package in R. A representative histogram obtained from RPB1-Ser2 ChIP from wild-type HeLa cells 3 h after 7 J/m^2 UV irradiation in Figure 4G.

(B) Time course of recovery index (RI) calculated for the 'central genic region' (from 5 kb downstream of TSS to 5 kb upstream of TES) of > 20 kb active genes. RI curves (calculated from the same data in Figure 5B) are nearly identical to those calculated for the entire gene. See Figure 5B for details.

(C) Time course of the denominator (dashed lines, *fwd* + *rev*) and the absolute value of the numerator (sold lines, |*fwd* - *rev*|) of the gene-by-gene SSI (RPB1-Ser2, 3E10, 7 J/m^2). These values were calculated as RPKM (reads per kilo base pairs per million) for the 'central genic region' of > 20 kb active genes. Medians of the individual values were plotted at each time point.

(D) Time course of median SSI (RPB1-Ser2) across relative position in gene bodies in whole active genes (central genic region of > 20 kb active genes) (3 h or earlier time points after 7 J/m^2 UV irradiation). See Figure 5C for details (3 h data replotted).

(E) Stalled RNAPIIo accumulation at T-T dimer (A < > A in the coding strand) sites in chr 1 (central genic region of > 20 kb active genes). The plot indicates abundance of ChIP-seq mapped reads in the coding strands adjacent to A < > A dimers in chr 1, due to the preferential amplification of undamaged strands. The data same as in Figure S5F (WT, RPB1-Ser2, 3E10, 3h after 7 J/m^2). RPGC represents 1x depth of coverage (reads per genome coverage).

(F) Time course of RPB1-Ser2 accumulation at T-T dimer (A < > A in the coding strand) sites 3 h or later after UV irradiation (central genic region of > 20 kb active genes, 3E10, 7 J/m^2). Results of earlier time points were shown in Figure 5D (3 h data replotted). RPGC represents 1x depth of coverage (reads per genome coverage).

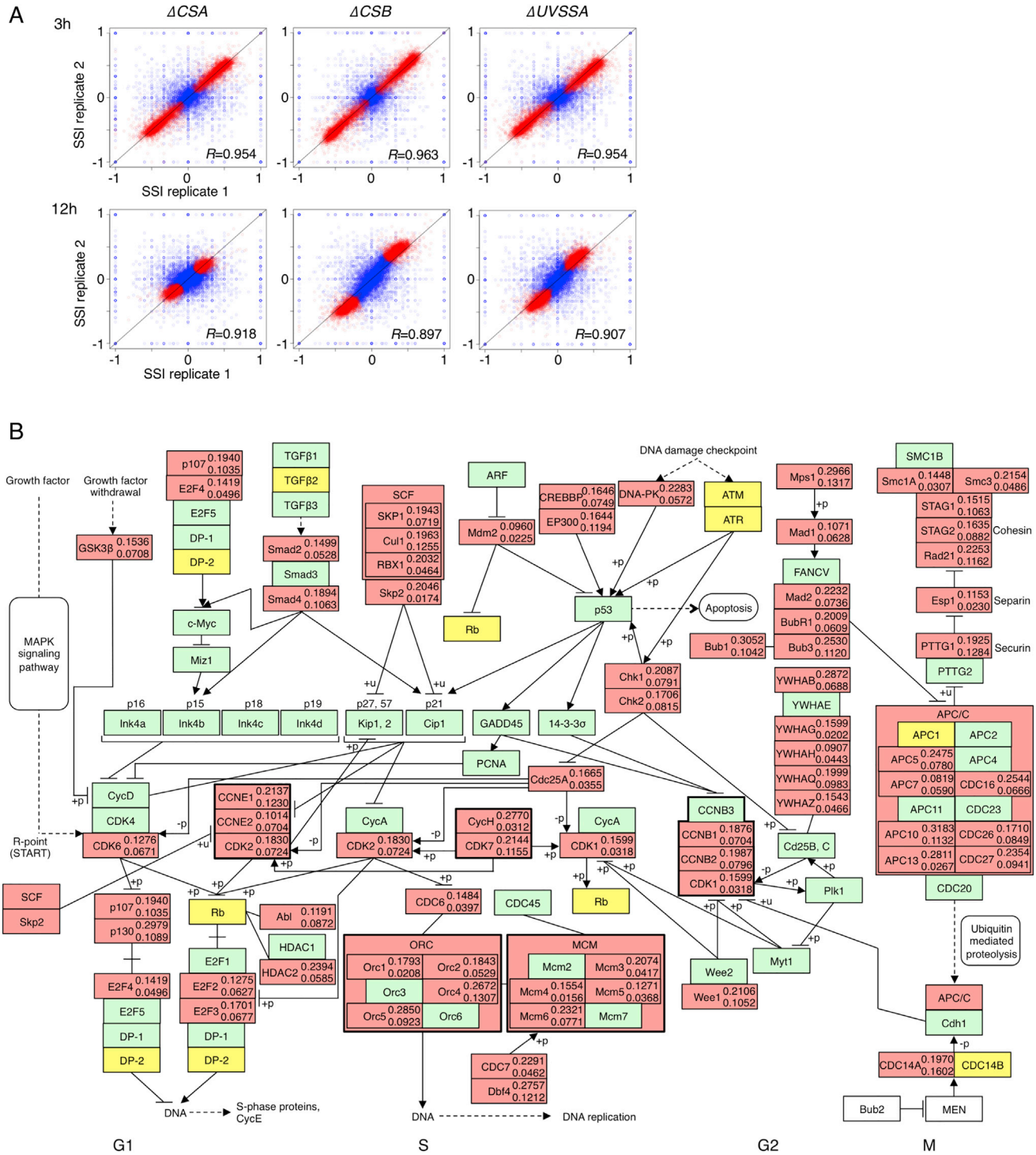

Figure S6. Gene-by-Gene Repair Profiles in TC-NER Mutants, Related to Figure 6

(A) Gene-by-gene correlation of SSI between biological replicates in Δ*CSA*, Δ*CSB*, and Δ*UVSSA* HeLa cells. See Figure 6A for details.

(B) A gene-enrichment analysis identified an accumulation of unrepaired genes in the 'cell cycle' pathway in RPB1-K1268R cells. Genes identified in Figure 6B (WT and RPB1-K1268R, 12 h after UV) were analyzed using the KEGG (Kyoto Encyclopedia of Genes and Genomes) database. Genes shown in reds are repaired in wild-type but unrepaired in RPB1-K1268R cells. SSIs for wild-type (bottom) and RPB1-K1268R (top) are shown. Genes in green, and yellow respectively represent repaired and unrepaired genes in both wild-type and RPB1-K1268R.

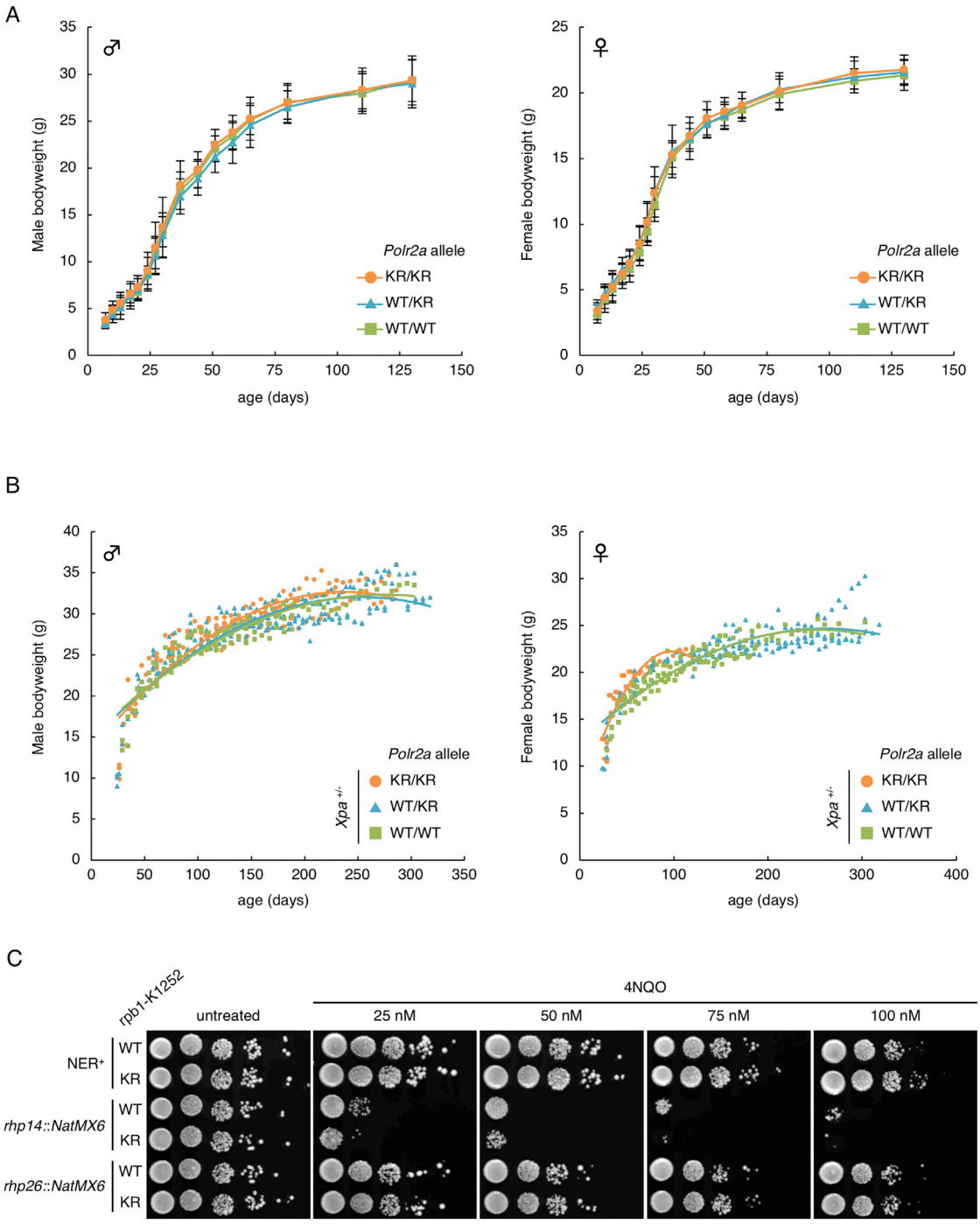

Figure S7. Phenotypes of *Polr2a*-K1268R and *rpb1*-K1252R, Related to Figure 7

(A) Growth curves of *Polr2a*$^{K1268R/K1268R}$ single mutant mice. No growth abnormality, in terms of bodyweight and lifespan, was observed in *Polr2a*$^{K1268R/K1268R}$ (KR/KR) and *Polr2a*$^{WT/K1268R}$ (WT/KR) compared to wild-type (WT/WT). Left panel, male; right panel, female. *Polr2a*$^{WT/WT}$ ♂ (n = 9); *Polr2a*$^{WT/KR}$ ♂ (n = 6); *Polr2a*$^{KR/KR}$ ♂ (n = 10); *Polr2a*$^{WT/WT}$ ♀ (n = 7); *Polr2a*$^{WT/KR}$ ♀ (n = 17); *Polr2a*$^{KR/KR}$ ♀ (n = 9). Body weights are presented as means (SD).

(B) Bodyweight distribution and growth curves of *Polr2a*$^{KR/KR}$ / *Xpa*$^{+/-}$ mice. *Xpa*$^{+/-}$ genotype is insufficient to induce high-load of endogenous DNA damage; *Polr2a*$^{KR/KR}$ / *Xpa*$^{+/-}$ mice did not elicit growth abnormality. WT/WT, *Polr2a*$^{WT/WT}$ / *Xpa*$^{+/-}$ (♂, n = 5; ♀, n = 6); WT/KR, *Polr2a*$^{WT/KR}$ / *Xpa*$^{+/-}$ (♂, n = 13; ♀, n = 14); KR/KR, *Polr2a*$^{KR/KR}$ / *Xpa*$^{+/-}$ (♂, n = 13; ♀, n = 6). Left panel, male; right panel, female.

(legend continued on next page)

(C) *S.pombe rpb1*-K1252R mutant displays a sensitivity to UV-mimetic 4NQO. Spot test analyses were performed on the *S. pombe rpb1*-K1252R strains with YES plates containing indicated concentrations of 4-Nitroquinoline 1-Oxide (4NQO). WT (*rpb1*$^{+}$) and KR respectively indicate the wild-type and K1252R RPB1 alleles. *rpb1*-K1252R *rhp14*::*NatMX6* double mutant displayed a synergistic effect. NER^{+}, NER-proficient; *rhp14*::*NatMX6*, Δ*XPA* homolog; *rhp26*:: *NatMX6*, Δ*CSB* homolog.